UCLA

Title

Reprogramming of nucleotide metabolism by interferon confers dependence on the replication stress response pathway in pancreatic cancer cells

Authors

Abt, Evan R
Le, Thuc M
Dann, Amanda M
et al.

Reprogramming of nucleotide metabolism by interferon confers dependence on the replication stress response pathway in pancreatic cancer cells

Evan R. Abt[1,2,13], Thuc M. Le[1,2,13], Amanda M. Dann[3,13], Joseph R. Capri[1,2], Soumya Poddar[1,2], Vincent Lok[1,2], Luyi Li[3], Keke Liang[4], Amanda L. Creech[1,2], Khalid Rashid[1,2], Woosuk Kim[1,2], Nanping Wu[3], Jing Cui[5], Arthur Cho[6], Hailey Rose Lee[1,2], Ethan W. Rosser[1,2], Jason M. Link[7], Johannes Czernin[1,2], Ting-Ting Wu[1], Robert Damoiseaux[1,8,9,10], David W. Dawson[11,12], Timothy R. Donahue[1,2,3,8,12,*], Caius G. Radu[1,2,8,14,*]

[1]Department of Molecular and Medical Pharmacology, University of California Los Angeles, Los Angeles, CA, USA

[2]Ahmanson Translational Theranostics Division, University of California Los Angeles, Los Angeles, CA, USA

[3]Department of Surgery, University of California Los Angeles, Los Angeles, CA, USA

[4]Department of General Surgery/Pancreatic and Thyroid Surgery, Shengjing Hospital of China Medical University, Shenyang 110004, China

[5]Department of Pancreatic Surgery, Tongji Medical College, Huazhong University of Science and Technology, Hubei, China

[6]Department of Nuclear Medicine, Yonsei University College of Medicine, Seoul 03722, South Korea

[7]Department of Molecular and Medical Genetics, Oregon Health and Science University, Portland, OR, USA

[8]Jonsson Comprehensive Cancer Center, University of California Los Angeles, Los Angeles, CA, USA

[9]California NanoSystems Institute, University of California Los Angeles, Los Angeles, CA, USA

[*]Correspondence: tdonahue@mednet.ucla.edu (T.R.D.), cradu@mednet.ucla.edu (C.G.R.).

[10]Department of Bioengineering, Samueli School of Engineering, University of California Los Angeles, Los Angeles, CA, USA

[11]Department of Pathology and Laboratory Medicine, University of California Los Angeles, Los Angeles, CA, USA

[12]David Geffen School of Medicine, University of California Los Angeles, Los Angeles, CA, USA

[13]These authors contributed equally

[14]Lead contact

SUMMARY

We determine that type I interferon (IFN) response biomarkers are enriched in a subset of pancreatic ductal adenocarcinoma (PDAC) tumors; however, actionable vulnerabilities associated with IFN signaling have not been systematically defined. Integration of a phosphoproteomic analysis and a chemical genomics synergy screen reveals that IFN activates the replication stress response kinase ataxia telangiectasia and Rad3-related protein (ATR) in PDAC cells and sensitizes them to ATR inhibitors. IFN triggers cell-cycle arrest in S-phase, which is accompanied by nucleotide pool insufficiency and nucleoside efflux. In combination with IFN, ATR inhibitors induce lethal DNA damage and downregulate nucleotide biosynthesis. ATR inhibition limits the growth of PDAC tumors in which IFN signalingis driven by stimulator of interferon genes(STING). These results identify a cross talk between IFN, DNA replication stress response networks, and nucleotide metabolism while providing the rationale for targeted therapeutic interventions that leverage IFN signaling in tumors.

In brief

Through orthogonal phosphoproteomic, metabolomic, and chemical genomics approaches, Abt et al. reveal that in pancreas cancer cells, type I interferon shifts nucleotide metabolism toward catabolism and activates the replication stress response kinase ATR. In combination with interferon signaling, ATR inhibition induces lethal DNA damage and limits PDAC tumor growth.

Graphical Abstract
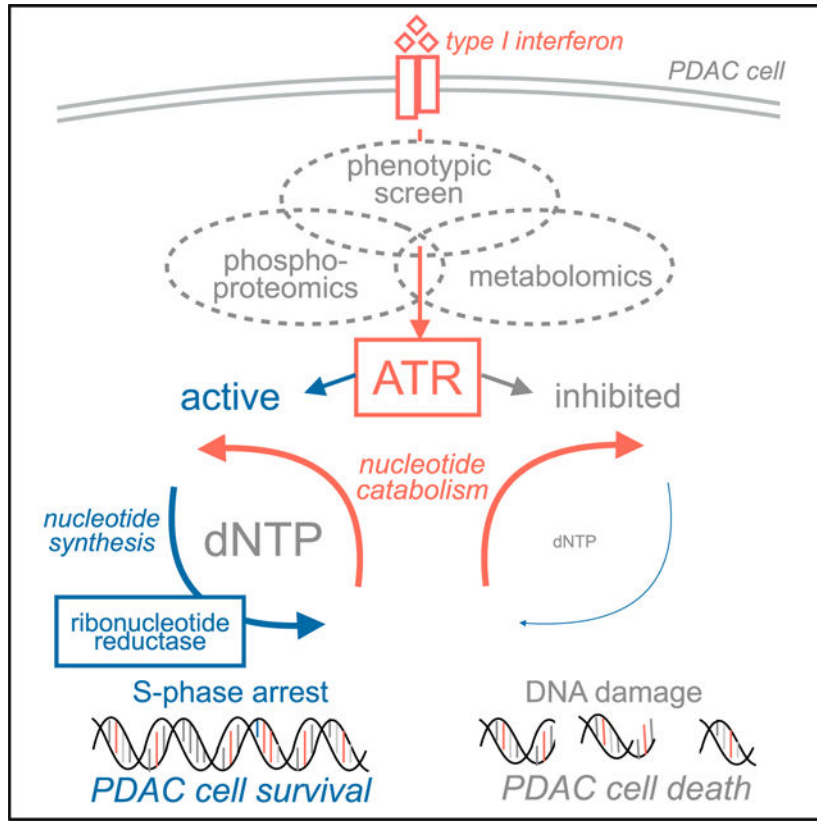
INTRODUCTION

Pancreatic ductal adenocarcinoma (PDAC) will become the second most common cause of cancer-related deaths in the United States by 2030 (Rahib et al., 2014). Contributing to this dismal prognosis is the resistance of PDAC tumors to current chemotherapy and immunotherapy regimens, indicating that a better understanding of fundamental PDAC tumor biology is required to inform the development and translation of more effective treatments (Kamisawa et al., 2016; Froeling et al., 2021). While an inflammatory, cytokine-rich tumor microenvironment is a hallmark of PDAC, whether tumor-cell-autonomous cytokine responses can be leveraged therapeutically has not yet been systematically investigated.

Among cytokines implicated in PDAC, interferons (IFNs) are particularly important as they influence cancer development and therapy responses through the transcriptional regulation of hundreds of IFN-stimulated genes (ISGs) (Parker et al., 2016). Type I IFNs, a multi-gene cytokine family that includes 13 IFNα subtypes in humans (14 in mice), IFNβ, IFNε, IFNτ, IFNκ, IFNω, IFNδ, and IFNζ, are produced by immune, stromal, epithelial, and tumor cells (Parker et al., 2016). All of these cell types are also capable of responding to type I IFNs, which function by binding and stimulating a dimeric receptor comprised of IFNAR1/IFNAR2, leading to the activation of a JAK1/TYK2 signaling cascade that initiates the ISGF3 transcription-factor-mediated transcriptional upregulation of ISGs (Cheon et al., 2013). Endogenous type I IFN production is governed by pattern recognition

receptor (PRR)-mediated pathways that detect pathogen-derived molecules or mislocalized self-nucleic acids (Vanpouille-Box et al., 2018). While decades of pre-clinical and clinical studies have investigated the potential of recombinant IFN to prime anti-cancer immunity, the development of synthetic PRR pathway activators, including agonists of Toll-like receptors (TLRs) and stimulator of IFN gene (STING), has provided novel approaches for therapeutic IFN stimulation (Ramanjulu et al., 2018).

Paradoxically, IFNs exert both pro- and anti-tumor effects. While IFN exposure impairs cancer cell proliferation *in vitro*, chronic IFN signaling *In vivo* is associated with radiation, chemotherapy, and immune checkpoint blockade resistance (Balkwill et al., 1978; Weichselbaum et al., 2008; Benci et al., 2019). Certain cancers display a constitutive expression of IFN signaling biomarkers, and there is mounting evidence that tumor cells themselves engender this cytokine response (Liu et al., 2019). In particular, a subset of PDACs have been recently shown to exhibit a tumor-cell-intrinsic IFN transcriptional program associated with a ductal cell of origin, hypomethylation of endogenous repetitive genomic elements, and constitutive PRR activation (Espinet et al., 2021).

Constitutive IFN signaling occurs in a significant subset of PDAC tumors, but its impact on tumor cells is incompletely understood and often overlooked. Furthermore, in contrast to the transcriptional effects of IFN which have been studied extensively, how these cytokines modulate tumor cell signaling networks and metabolism is much less well-characterized. In leukemia cells, IFNs alter nucleotide metabolism by decreasing the abundance of nucleotides; however, the molecular mediators of this effect remain uncharacterized, and whether this occurs in solid tumors has not yet been determined (Barankiewicz et al., 1986). The effect of IFNs on nucleotide levels may be particularly important as a balanced and sufficient supply of deoxyribonucleotide triphosphate (dNTP) pools is essential for sustaining cancer cell DNA replication and repair (Le et al., 2017). To survive dNTP insufficiency, cancer cells rely on the replication stress-response signaling pathway, which is triggered by impaired DNA replication in S-phase (Zeman and Cimprich, 2014). The proximal mediator of this response, ataxia telangiectasia and Rad3-related protein (ATR), initiates a protein-kinase-mediated signaling cascade that halts DNA replication by suppressing origin firing, promotes replication fork stabilization, and activates an intrinsic S/G2 checkpoint (Brown et al., 2017; Saldivar et al., 2018). Additionally, ATR promotes *de novo* nucleotide biosynthesis by both transcriptional and post-translational induction of ribonucleotide reductase (RNR), which catalyzes the conversion of ribonucleotides to deoxyribonucleotides (Zhang et al., 2009; D'Angiolella et al., 2012). ATR also facilitates the salvaging of pre-formed environmental nucleosides for dNTP synthesis through the activation of deoxycytidine kinase (dCK) by phosphorylation of serine 74 (Beyaert et al., 2016). Clinically, ATR has emerged as a promising target in cancer therapy, and several ATR inhibitors are currently being evaluated alongside chemotherapy, radiation, and PARP inhibition for the treatment of tumors exhibiting high levels of intrinsic replication stress (Lecona and Fernandez-Capetillo, 2018).

Here, we determined that a subset of PDAC patient- and cell-line-derived xenograft tumors exhibit an intrinsic IFN response that is not modeled by standard cell culture conditions. Through the integration of orthogonal phosphoproteomic, metabolomic, and chemical

genomic assays, we determined that IFN signaling causes PDAC cells to rely on replication stress-response signaling for survival. Inhibiting the proximal mediator of this pathway, ATR, in IFN-exposed PDAC cells induces catastrophic DNA damage and apoptosis. IFN upregulates multiple genes involved in nucleotide/nucleoside catabolism such as sterile alpha motif and HD domain-containing protein 1 (SAMHD1), 5′-nucleotidase cytosolic IIIA, (NT5C3A), and thymidine phosphorylase (TYMP). In combination, IFN signaling and ATR inhibition restrict the utilization of dNTPs for DNA replication by promoting their breakdown and impairing their biosynthesis. *In vivo*, ATR inhibition limits the growth of PDAC tumors with enhanced IFN signaling driven by tumor cell-intrinsic activation of STING. This study highlights a previously unappreciated functional crosstalk between cytokine signaling, nucleotide metabolism, and the DNA replication stress-response pathway in PDAC and identifies ATR as an IFN-driven collateral dependency that can be leveraged therapeutically by small-molecule inhibitors currently under clinical investigation.

RESULTS

IFN signaling is constitutive in a subset of PDAC tumors

A subset of PDAC tumors in The Cancer Genome Atlas (TCGA) dataset exhibit enriched expression of a previously defined IFN-response gene expression signature (Figure 1A) (Cancer Genome Atlas Research Network, 2017; Doherty et al., 2017). IFN response genes were co-expressed across samples but not preferentially enriched among tumors consistently defined as classical or squamous PDAC subtypes (Figures 1A and S1A) (Bailey et al., 2016; Collisson et al., 2011; Moffitt et al., 2015). These findings were confirmed using an expanded IFN-response gene set (Figure S1B). Likewise, a subset of primary tumors and patient-derived specimens from our institution expressed high levels of two canonical surrogate markers of type I IFN signaling, STAT1 and MX1, which were notably localized to tumor cell compartments rather than the surrounding stroma as determined by immunohistochemistry (IHC) (Figures 1B and 1C) (Rusinova et al., 2013). Furthermore, IHC profiling of a library of 33 primary patient-derived PDAC xenograft tumors derived at our institution and 17 PDAC cell line xenograft tumors indicated that the majority of specimens exhibited high levels of STAT1 and MX1 immunoreactivity with a minority scoring as low or negative and that the expression of these markers were positively correlated (Figure 1D) (Moore et al., 2021). In contrast to the *In vivo* setting where MX1 and STAT1 were highly expressed, PDAC cells lacked ISG expression when grown as monolayer cultures *in vitro*; however, IFNβ (IFN) treatment induced ISG expression in all tested models (Figures 1E and S1C). Taken together, these findings indicate that IFN signaling occurs constitutively in a subset of PDAC tumors and that it can be modeled in cell cultures through IFN supplementation.

The replication stress response pathway is a collateral dependency triggered by IFN

We next explored the possibility that IFN exposure elicits targetable, tumor-supportive adaptive signaling vulnerabilities in PDAC cells that are not revealed by *in vitro* cancer cell line codependency-screening approaches in which cytokines, including IFN, are generally omitted. We reasoned that such adaptive mechanisms could be identified and prioritized by intersecting two orthogonal approaches measuring: (1) IFN-induced protein

kinase activation using nanoscale liquid chromatographic tandem mass spectrometry (nLC-MS/MS) phosphoproteomics and (2) IFN-induced protein kinase dependency using a chemical genomics phenotypic screen (Figures 2A and 2B). Phosphoproteomic analysis of SUIT2 PDAC cells 24 h after IFN stimulation identified 943 significantly altered proteins (among 6,668 detected, at 1% false discovery rate [FDR]) and 911 significantly altered phosphopeptides (among 17,368 detected, at 0.1% FDR). As expected, IFN enhanced the protein levels of annotated ISGs (Figure S2A). Kinase-substrate enrichment analysis (KSEA) (Wiredja et al., 2017) of phosphopeptides significantly altered by IFN identified enriched phosphorylation of replication stress-response kinase ATR substrates alongside ataxia telangiectasia-mutated (ATM), homeodomain-interacting protein kinase 2 (HIPK2), and MAPK1/3 (ERK1/2) substrates. We observed that while IFN increased the abundance of phosphorylated peptides corresponding to ATR targets (CHEK1, FANCD2, BRCA1, NBN), their protein levels were unchanged, which indicates increased ATR kinase activity (Figure 2A). In parallel, we performed a chemical genomics phenotypic screen to identify actionable adaptive signaling codependencies triggered by IFN exposure (Figure 2B). Among a library of 430 protein kinase inhibitors, modifiers of replication stress-response kinases including ATR (AZD-6738 [Foote et al., 2018]) and its downstream effector kinase CHEK1 (LY2603618, PF-477736, and AZD-7762 [Brown et al., 2017]) exhibited significantly increased anti-proliferative activity against IFN-treated SUIT2 cells. Conversely, JAK inhibitors (LY278544, tofacitinib, and ruxolitinib [Schwartz et al., 2017]), which block type I IFN signaling, abrogated IFN-induced proliferation inhibition (Figure 2B).

Findings from the phosphoproteomics and the small-molecule kinase inhibitor screens consistently identified a functional link between IFN exposure and the replication stress-response signaling pathway. IFN exposure led to ATR activation, as evidenced by enhanced substrate phosphorylation, and it sensitized PDAC cells to inhibitors of ATR or its downstream effector kinases CHEK1 and WEE1 (Figures S2B and S2C). We confirmed IFN-induced activation of the replication stress response using an immunoblot analysis in which enhanced CHEK1-S345 phosphorylation was observed 12 h after the addition of IFN in SUIT2 cells (Figure S2D). Consistently, IFN triggered S-phase accumulation, a phenotype associated with replication stress, as determined by 5-ethynyl-2′-deoxyuridine (EdU) labeling and flow cytometry (Figure S2E).

To further investigate the effects of the IFN/ATR inhibitor combination, we evaluated alterations in single-stranded DNA (ssDNA) abundance, an established consequence of replication fork stalling and replication stress (Le et al., 2017). While either IFN or ATR inhibition triggered ssDNA accumulation in SUIT2 cells, the greatest degree of induction was observed following combination treatment (Figure 2C). Additionally, IFN alone induced a minor (~3%) increase in the percentage of phosphorylated H2A.X-S139-positive cells, a marker of DNA damage caused by unresolved replication stress, but triggered a much higher increase (to over 60% pH2A.X-S139-positive cells) when administered alongside an ATR inhibitor (Figure 2D). Consistently, apoptosis was synergistically induced by the IFN and ATR inhibitor combination as determined by an immunoblot analysis for Cleaved Caspase3/PARP and Annexin V/propidium iodide (PI) flow cytometry (Figures 2E and 2F).

Next, we evaluated the link between IFN exposure and ATR activation across a panel of PDAC cell lines and observed varying degrees of IFN-induced CHEK1-S345 phosphorylation (Figure 2G). Additionally, CellTiter-Glo cell proliferation and flow cytometry cell-cycle analyses revealed heterogeneous degrees of IFN-induced S-phase accumulation and a sensitization to ATR inhibitors across PDAC cell lines (Figure 2H). IFN most potently enhanced the effects of ATR inhibition in models exhibiting the greatest degree of IFN-induced S-phase accumulation and CHEK1-S345 phosphorylation, suggesting that IFN-induced replication stress is a direct cause of ATR inhibitor sensitization (Figures 2G and 2H). Consistent with the CellTiter-Glo analysis, Incucyte live-cell imaging indicated that while single-agent IFN or ATR inhibition alone moderately slowed growth, the combination completely blocked proliferation (Figure S2F). Furthermore, IFN treatment potentiated S-phase arrest, proliferation inhibition, and apoptosis induced by ATR inhibition in A31A primary human PDAC cells (Figures S2G, S2H, and S2I), whereas no significant anti-proliferative effects nor S-phase arrest was observed in human pancreatic ductal epithelial cells (Ouyang et al., 2000), which possess a doubling time similar to SUIT2 and a nearnormal genotype (Figures S2J and S2K).

In tumor microenvironments, type I IFNs co-exist with additional cytokines produced by immune and stromal cells, including type II IFN (IFNγ), which is primarily produced by activated T cells and natural killer (NK) cells. To determine if PDAC cell CHEK1 phosphorylation is altered in the context of an endogenous cytokine response, we isolated conditioned media from human peripheral blood mononuclear cells (PBMCs) treated with T cell mitogens (phytohemagglutinin [PHA] and interleukin-2 [IL-2]) to induce T cell activation. Activated PBMC-derived conditioned media induced the expression of the ISG STAT1 in PDAC cells and enhanced CHEK1-S345 phosphorylation (Figure S2L). Recombinant IFNγ also triggered CHEK1-S345 phosphorylation (Figure S2L) and synergized with ATR inhibition to induce apoptosis (Figure S2M). Collectively, these results indicate that both type I and II IFNs activate the DNA replication stress-response pathway in PDAC cells and render them sensitive to ATR inhibition.

IFN signaling augments nucleotide catabolism

To investigate whether activation of the replication stress-response pathway in tumor cells by IFN is associated with metabolic alterations, we used LC-MS to measure >450 metabolites in two cell lines (SUIT2 and YAPC) in which IFN induces ATR activation in response to IFNβ and in one (PANC1) that does not. IFN altered the levels of a greater number of metabolites in sensitive SUIT2 and YAPC cells than in resistant PANC1 cells, which associate with the separation of these models along the PC2 axis in principal-component analysis (PCA; Figure 3A). Metabolite set enrichment analysis (MSEA [Xia and Wishart, 2010]) of significantly altered metabolites identified multiple processes related to nucleotides including purine, pyrimidine, and NAD^+ metabolism, which were significantly altered by IFN (Figure 3B). The impact of IFN on NAD^+/NADH levels is consistent with previous reports showing that IFNγ inhibits tumor cell growth via NAD depletion and that type I IFN is linked to NAD^+ pool alterations in tumor cells via upregulation of non-canonical PARPs (Aune and Pogue, 1989; Moore et al., 2021).

IFN decreased the levels of multiple biosynthetic intermediates and end-products in pyridine, purine, and pyrimidine nucleotide synthesis while simultaneously increasing metabolites generated from their catabolism (Figure 3C). Although all three PDAC models displayed altered nucleotide and NAD^+/NADH pools following exposure to IFN, we noted significant heterogeneity in both the basal levels and the magnitude of decrease in these metabolites of responses to IFN (Figure 3D); this heterogeneity may reflect unique genetic features that confer a differential capacity to tolerate perturbations of nucleotide metabolic pathways, as previously described in the context of NAD^+ depletion (Xiao et al., 2016). Accordingly, in PANC1 cells, baseline dNTP and NAD^+/NADH pool levels were substantially higher than those in SUIT2 and YAPC cells (Figure 3D). Additionally, the magnitude of the IFN-induced decreases in dNTP and NAD^+/NADH pools was lower in PANC1 than in SUIT2 or YAPC cells (Figure 3D).

Since dNTP insufficiency is a major cause of DNA replication stress, we aimed to further understand the links between IFN signaling and alterations in the levels of key intermediates involved in the biosynthesis and breakdown of nucleotides. Decreases in dNTP abundance may be a consequence of either impaired biosynthesis, increased consumption, or enhanced catabolism. To identify potential mechanisms responsible for dNTP pool restriction triggered by IFN, we adapted a targeted LC-MS/MS-multiple reaction monitoring (MRM) approach previously reported by our group (Le et al., 2017; Abt et al., 2020) to evaluate alterations in the contribution of stable-isotope-labeled glucose ($[^{13}C_6]$glucose) to: (1) intracellular nucleotide pools, (2) extracellular nucleosides (the products of rNTP/dNTP hydrolysis), and (3) dNTP consumption for DNA replication (Figure 4A). This targeted assay consistently revealed IFN-induced decreases in dCTP, dTTP, dATP, and dTTP pool levels in addition to a restriction of the incorporation of $[^{13}C_6]$glucose-derived nucleotides to newly synthesized DNA (Figure 4A). IFN simultaneously induced the efflux of $[^{13}C_6]$glucose-derived deoxycytidine (dC), cytidine (rC), and uridine (rU) into the extracellular space (Figure 4A). Purine nucleosides were undetectable in culture media, which is likely the result of rapid catabolism by adenosine deaminase (ADA) or purine nucleoside phosphorylase (PNP) (Camici et al., 2019; Le et al., 2017). dNTP pool restriction was not a transient response to IFN exposure, as reductions were observed in SUIT2 cells after 21 days of chronic IFN exposure (Figure S3A). Collectively, our findings indicate that IFN remodels nucleotide catabolism.

To identify candidate genes that may mediate the shift toward nucleotide/nucleoside catabolism induced by IFN exposure, we probed our global proteomics dataset (Figure 2A)for IFN-regulated proteins involved in nucleotide and nucleoside metabolism. Notably, multiple proteins related to these processes, including SAMHD1 (which catalyzes dNTP phosphohydrolysis) (Goldstone et al., 2011); TYMP (which catalyzes the first step in thymidine catabolism) (Liang et al., 2021); NT5C3A (a nucleotidase which converts UMP and CMP to rU and rC, respectively) (Bianchi and Spychala, 2003); and VIPERIN (also known as RSAD2, which converts CTP to 3′-deoxy-3′,4′-didehydro-CTP [ddhCTP], a naturally occurring anti-viral factor) (Gizzi et al., 2018) were significantly upregulated in IFN-treated cells (Figures 4B and S3B). Furthermore, IFN downregulated dihydrofolate reductase (DHFR) and thymidylate synthase (TYMS), two essential mediators of *de novo* nucleotide synthesis. Immunoblot analysis confirmed IFN-induced alterations on the levels

of these nucleotide metabolism regulators (Figure 4C). These results indicate that IFN coordinates a multigene metabolic program that alters the balance between catabolic and anabolic processes in nucleotide metabolism, thereby triggering dNTP pool insufficiency and replication stress in PDAC cells (Figure 4D).

SAMHD1 emerged as a potential mediator of IFN-induced dNTP alterations as it catalyzes intracellular dNTP phosphohydrolysis to deoxyribonucleosides (dNs) that may then be effluxed across the plasma membrane via equilibrative nucleoside transporters. To investigate the role of SAMHD1 in IFN-induced nucleotide pool restriction, we generated SAMHD1-knockout (KO) SUIT2 cells using CRISPR-Cas9 and applied our LC-MS/MS-MRM assay to evaluate the contribution of $[^{13}C_6]$glucose to dNTP pools, extracellular dNs, and newly replicated DNA in this model (Figures 4E and S3C). In SAMHD1-proficient cells, IFN treatment resulted in a 2-fold decrease in dCTP levels and a 3-fold increase in dC efflux (Figure 4E). In contrast, SAMHD1-KO cells, which at baseline possess a nearly 3-fold larger labeled dCTP pool than parental cells, were not impacted by IFN in terms of their dCTP pools or dC efflux. While IFN treatment decreased the contribution of $[^{13}C]$glucose-labeled dCTP (generated via the *de novo* pathway) to newly synthesized DNA in both parental and SAMHD1-KO cells, indicating a reduction in the rate of S-phase progression, this effect was significantly less pronounced in KO cells (Figure 4E). Moreover, genetic SAMHD1 inactivation increased baseline dATP pools and partially rescued IFN-induced dATP restriction (Figure 4E). Prompted by these observations, we attempted to rescue IFN-induced ATR activation and S-phase arrest by supplementing cells with various ribonucleosides or dN substrates for nucleoside salvage pathways as well as with dNTPs. None of our nucleoside or nucleotide supplementation schemes counteracted IFN-induced ATR activation (Figure S3D). Given that NAD$^+$/NADH reductions were observed following IFN treatment and that these factors fuel PARylation reactions that are required for the recruitment of ssDNA break repair proteins such as XRCC1 (El-Khamisy et al., 2003) and enable the activity NAD$^+$-dependent sirtiun-1 (SIRT1), which has DNA repair functions (Alves-Fernandes and Jasiulionis, 2019), we also evaluated nicotinamide riboside (NR) supplementation, which restored NAD$^+$/NADH pools in IFN-treated cells but did not prevent CHEK1-S345 phosphorylation (Figure S3E). The inability of an exogenously added dNTP precursor to rescue IFN-induced alterations in cell-cycle progression may be explained by the impact of catabolic genes (including those regulated by IFN) on the metabolic fates of exogenously added nucleosides. Thymidine is catabolized by TYMP, which is itself an ISG. Purine nucleosides are readily catabolized to nucleobases (hypoxanthine and guanine) byADA andPNP. These nucleobases can be recycled by hypoxanthine phosphoribosyltransferase (HPRT) to generate purine ribonucleotides, which, following their conversion to dNTPs, may additionally be susceptible to degradation by SAMHD1.

Collectively, these findings indicate that dNTP pool insufficiency and impaired DNA replication induced by IFN likely reflect the combined effects of multiple alterations in nucleotide metabolism that cannot be compensated for by increasing the flux through nucleoside salvage pathways via substrate supplementation (Figure 4D).

ATR inhibitors and IFN cooperatively restrict dNTP pools

As ATR has been shown to regulate both *de novo* and scavenging nucleotide synthesis via transcriptional and post-translational mechanisms, we reasoned that ATR inhibition could enhance dNTP restriction triggered by IFN (Le et al., 2017). LC-MS/MS analysis revealed that while both IFN and ATR inhibition decreased dCTP levels alone, the combination elicited the greatest effect (Figure 5A). To evaluate the impact of IFN and ATR inhibition on DNA replication dynamics, we tracked the incorporation of [$^{13}C_6$]glucose into nucleosides in newly replicated DNA using LC-MS/MS-MRM. Both IFN exposure and ATR inhibition decreased the contributions of the *de novo* pathway to dCTP incorporated into newly replicated DNA, and the greatest degree of inhibition was observed in combination-treated cells (Figure 5B). This reduction is consistent with increased DNA damage identified in combination-treated cells in Figure 2D and may reflect replication fork collapse or delays in restarting DNA replication following ATR inhibition. ATR promotes *de novo* dNTP synthesis by transcriptional and post-translational regulation of RNR regulatory subunit M2 (*RRM2*), the S-phase restricted catalytic subunit of RNR (Zhang et al., 2009; D'Angiolella et al., 2012). ATR-mediated stabilization of the transcription factor E2F1 facilitates *RRM2* expression, and ATR activation prevents SCF^{CyclinF} ubiquitin ligase complex-dependent *RRM2* degradation triggered downstream of *RRM2*-T33 phosphorylation by CDK1. In SUIT2 cells, ATR inhibition decreased the protein levels of E2F1 and its *de novo* nucleotide synthesis-related targets *RRM2*, RRM1, and thymidine kinase 1 (TK1) (Figure 5C). Consistently, ATR inhibition restricted *RRM2* transcript levels (Figure 5D)and proteasome inhibition partially rescued ATR-inhibitor-mediated *RRM2* downregulation, indicating that in this model ATR functions to promote RNR activity through both translational and post-transcriptional mechanisms (Figure 5E). ATR inhibition only decreased *RRM2* protein levels in cell lines in which IFN potentiated the anti-proliferative effects of ATR inhibitors (SUIT2 and DANG) but not in PANC1 cells (Figure 5F). Consistently, the combination of IFN and ATR inhibition synergistically triggered S-phase accumulation, a phenotype associated with dNTP insufficiency, in SUIT2 and DANG cells but not in PANC1 cells (Figure 5G). These results indicate that while IFN restricts dNTP abundance by initiating nucleotide and nucleoside catabolism, ATR inhibition primarily restricts dNTP levels via downregulation of genes required for *de novo* dNTP biosynthesis.

Tumor cell-autonomous IFN signaling driven by STING sensitizes PDAC cells to ATR inhibition

We next aimed to determine whether autocrine/paracrine IFN signaling initiated by PDAC cells phenocopies recombinant IFN treatment and drives sensitization to ATR inhibitors. Our observation of ISG enrichment in the majority of patient-derived and PDAC cell line xenograft tumors implicated tumor cells themselves as a source of IFN signaling as IFNs are species restricted. Type I IFN production is initiated downstream of the activation of various nucleic-acid-sensing mechanisms. One such sensor is cyclic GMP-AMP synthase (cGAS), which binds cytosolic double-stranded DNA and, in turn, activates STING via production of the cyclic dinucleotide second messenger 2'–3'-cGAMP (Motwani et al., 2019). While most nucleic acid sensors are predominantly expressed in immune cells, the cGAS/STING pathway is broadly expressed in immune, stromal, endothelial, and epithelial cells as well as in certain cancers. In contrast to other tumor types in which cGAS and STING are

suppressed, STING is expressed in PDAC tumors compared with normal pancreatic tissue (Figure 6A). Moreover, IHC analyses of a PDAC tissue microarray derived at our institution revealed detectable STING expression in tumor cells at varying levels in >90% of samples, a finding consistent with a previous report(Figure 6B)(Baird et al.,2016). Thus, we further investigated the potential of cGAS/STING pathway stimulation to elevate IFN signaling responses in PDAC tumors.

IFNB1 transcript levels were induced in a subset of PDAC cell lines following transfection with the cGAS ligand IFN stimulatory DNA (ISD), thereby confirming cGAS/STING pathway functionality (Figure S4A). Each of the models responsive to ISD expressed both cGAS and STING (Figure S4A). Despite expressing both cGAS/STING, SUIT2 cells failed to respond to ISD stimulation. However, in SUIT2 cells, the *IFNB1* transcript was induced when STING was directly activated by transfection with a biphosphorothioate cGAMP-analog (Figure S4B). As expected, cGAMP transfection triggered activation of proximal STING signaling (evidenced by IRF3-S396 phosphorylation), autocrine IFN signaling (evidenced by STAT1-Y701 phosphorylation), and ISG expression in STING-expressing SUIT2 and DANG cells (Figure S4C). Inhibition of JAK using ruxolitinib abrogated cGAMP-induced STAT1 phosphorylation and ISG induction but not IRF3-S396 phosphorylation. IFNβ was detected in PDAC cell-culture supernatants following cGAMP transfection (Figure S4D). As the cGAS/STING pathway drives autocrine/paracrine IFN signaling and is functional in a subset of PDAC cells, we reasoned that it could initiate the IFN signaling response observed in xenograft tumors (Figures 1D and 1E). To investigate this possibility, we used CRISPR-Cas9 to KO STING in HS766T, DANG, and CFPAC1 cells, which exhibit constitutive ISG expression when grown as xenograft tumors in immunodeficient mice. Immunoblot analyses indicated that STING KO eliminated ISG expression in HS766T and DANG xenograft tumors (Figure 6C). However, ISG expression in CFPAC1 xenograft tumors was not affected by STING KO, indicating that an additional mechanism sustains ISG expression in this model (Figure S4E). Collectively, these results indicate that the cGAS/STING pathway drives constitutive IFN signaling in a subset of xenograft tumors and that autocrine IFN signaling can be induced downstream of STING activation in PDAC cells.

To determine whether STING-driven autocrine IFN signaling sensitizes PDAC cells to ATR inhibition, we employed SUIT2 cells engineered to express a constitutively active STING mutant (SUIT2-TetR-STING^{R284M}) conditionally in the presence of doxycycline (Tang and Wang, 2015). SUIT2 cells were chosen for this model as they did not exhibit constitutive expression of ISGs when grown as tumors in mice but were responsive to IFN (Figure S5A). Live-cell imaging of anchorage-independent SUIT2-TetR-STING^{R284M} cultures indicated that while doxycycline-initiated STING activation and ATR inhibition individually impaired sphere growth, the combination completely prevented proliferation (Figure 6D). JAK signaling was essential for this synergy, as ruxolitinib restored the proliferation of combination-treated cells (Figure S5B). In a second conditional model using YAPC-TetR-STING^{R284M} cells, genetic STING activation elicited JAK-dependent ISG expression (Figure S5C) and sensitized cells to ATR inhibition (Figure S5D). Furthermore, treatment with the small-molecule STING agonist diABZI-compound 3 (Ramanjulu et al.,

2018) enhanced the anti-proliferative effects of AZD-6738 in SUIT2 and CFPAC1 cells (Figure S5E).

Analysis of SUIT2-TetR-STING^{R284M} tumors isolated from mice treated with doxycycline and the ATR inhibitor AZD-6738 (Foote et al., 2018) revealed that STING activation induced ISG (MX1) expression and ATR-dependent CHEK1-S345 phosphorylation (Figure 6E). AZD-6738 treatment additionally restricted the growth of STING-active subcutaneous and orthotopic SUIT2-TetR-STING^{R284M} tumors (Figures 6F, 6G, and 6H). Collectively, these findings indicate that genetic or pharmacological STING activation induces IFN signaling, triggers ATR activation, and sensitizes PDAC cells to pharmacological ATR inhibition.

DISCUSSION

Here, we provide new insight into the consequences of IFN signaling in PDAC cells. Using orthogonal phosphoproteomics and chemical genomics approaches, we identified the replication stress-response pathway as an IFN-induced collateral dependency in a subset of PDAC cells. Inhibition of the replication stress-response kinase ATR induces replication catastrophe in IFN-treated PDAC cell lines and primary cells but not in non-transformed cells. We found that IFN regulates a metabolic program that controls the abundance of intracellular nucleotide pools by stimulating their catabolism to nucleosides, which are in turn released into the environment. Mechanistically, ATR inhibition restricts the expression of *RRM2*, a rate-limiting mediator of *de novo* dNTP synthesis, and enhances IFN-induced depletion of nucleotide pools. Additionally, we determined that the cGAS/STING pathway is active in PDAC cells and is required for constitutive type I IFN signaling in a subset of xenograft tumors. Furthermore, we demonstrated that ATR inhibition restricts the growth of subcutaneous and orthotopic PDAC tumors in which IFN signaling is driven by STING activation.

The ATR inhibitors ceralasertib (AstraZeneca, also known as AZD-6738), berzosertib (EMD Serano, also known as VE-822), and BAY1895344 (Bayer) are currently being evaluated for the treatment of DNA-damage response (DDR)-deficient cancers or in combination with chemotherapy, PARP inhibitors, and immune checkpoint blockade for solid tumors including PDAC (Brown et al., 2017). In our study, a range of responses to the IFN/ATR inhibitor combination across PDAC models was observed, which is likely reflective of the well-documented genomic, transcriptional, and metabolic heterogeneity of this disease (Collisson et al., 2011; Daemen et al., 2015) (Figure 2H). Tumor-cell-intrinsic factors, such as DDR defects or KRAS, TP53, or ARID1A mutations, and intrinsic replication stress may also dictate the efficacy of pharmacological ATR inhibition (Brown et al., 2017). Furthermore, dNTP synthesis capacity critically dictates the requirement for ATR, as increasing RNR activity can rescue ATR-deficiency-induced genomic fragile-site breakage in mice, and pharmacological RNR inhibition amplifies the anti-tumor activity of ATR inhibitors (Lopez-Contreras et al., 2015; Le et al., 2017). *In vivo*, the degree of replication stress and sensitivity to replication stress-response inhibitors is likely dictated by not only constitutive IFN signaling but also by oncogene activation, metabolite availability, and reactive oxygen species levels (Lecona and Fernandez-Capetillo, 2018).

An early study of IFN responses in cancer cells reported alterations in nucleotide metabolism (Barankiewicz et al., 1986). Our findings build on this foundational observation and demonstrate that IFN upregulates the expression and activity of multiple mediators of nucleotide metabolism including SAMHD1, which catalyzes dNTP phosphohydrolysis to nucleosides. Notably, environmental dC produced by pancreatic stellate cells and tumor-resident macrophages limits the efficacy of gemcitabine by competing for phosphorylation by dCK (Halbrook et al., 2019; Dalin et al., 2019). Our findings indicate that cancer cells may be an additional source of dC and implicate IFN and SAMHD1 as critical regulators of its abundance. Beyond tumor cells, we have determined that IFN induces SAMHD1 expression and enhances dC efflux in a PDAC-cancer-associated fibroblast model (Figure S6). Additionally, IFN-induced nucleoside release may be counteracted by nucleoside salvage kinases such as dCK, TK1, and uridine cytidine kinases (UCKs), which enable the conversion of pyrimidine nucleosides to nucleotides (Le et al., 2017). Beyond their role as metabolic precursors, the nucleosides uridine and guanosine have been identified as co-ligands for endosomal TLR7 and TLR8, respectively, indicating that IFN-stimulated nucleoside efflux may also generate ligands for these receptors (Zhang et al., 2016; Tanji et al., 2015).

The low-grade chronic inflammatory response observed in PDAC has been referred to as "para-inflammation" and is defined by a transcriptional signature resembling the type I IFN response (Aran et al., 2016). Among TCGA datasets, PDAC ranks the highest in terms of para-inflammation signature enrichment, which is a negative prognostic factor (Aran et al., 2016). Consistently, a tumor-cell-intrinsic IFN transcriptional program has been identified in a subset of PDACs and is associated with an aggressive phenotype (Espinet et al., 2021). Regarding the discrepancy between basal ISG expression in PDAC cell lines *in vitro* and *in vivo*, models exhibiting intrinsic IFN biomarker expression when grown as tumors may constitutively release minimal amounts of IFN that are insufficient to drive intrinsic signaling *in vitro*, as IFNs can be diluted in culture media and eliminated by routine cell passaging. A second explanation is that the stimulus responsible for intrinsic IFN signaling, potentially a nucleic acid sensor ligand, is present *In vivo* but absent *in vitro*. Beyond cGAS/STING, the roles of additional type I IFN-inducing pathways, such as those regulated by TLRs and MDA5/MAVS, to tumor-intrinsic IFN signaling are unclear and will require additional studies. While we focused our investigation on PDAC, IFN-signaling transcriptional signature enrichment has been implicated in other malignancies such as inflammatory breast and bladder cancers (Provance and Lewis-Wambi, 2019; Aran et al., 2016). Whether tumor-cell-autonomous STING signaling drives this IFN response or if ATR inhibitors are potentiated by IFN in these settings remains to be determined.

Limitations of the study

A limitation of this study is the reliance on recombinant type I IFN to stimulate PDAC cell responses *in vitro*. In tumor microenvironments, IFNs are a component of multi-faceted cytokine responses mediated by various cell types including immune cells (Parker et al., 2016). We have shown that conditioned media from activated human PBMCs triggers CHEK1 phosphorylation in PDAC cells and that IFNγ also sensitizes PDAC cells to ATR inhibition. This finding may be linked to pre-clinical observations associating

pharmacological ATR inhibition with increased antitumor activity of CD8^{+} T cells (Vendetti et al., 2018). Additionally, we utilized a recently developed STING agonist (Ramanjulu et al., 2018) and linked both genetic and pharmacological STING activation to increased IFN signaling and ATR inhibitor sensitization in PDAC cells (Figure S5E). As systemic STING agonists are advancing in the clinic for the treatment of solid tumors including PDAC, understanding their direct and indirect (cytokine-mediated) effects on tumor cells should be prioritized, and it remains to be determined whether basal IFN signaling in tumors influences the outcomes of STING agonist treatment. Regarding the link between IFN signaling, nucleotide metabolism, and replication stress, the identification of a single ISG mediator of our observed metabolic and phenotypic alterations is a significant challenge, as multiple IFN-regulated genes related to both the synthesis and breakdown of nucleotides were identified. In addition to IFN-regulated metabolic genes, the ISG promyelocytic leukemia gene (PML) has been linked to delays in S-phase progression and could indirectly mediate nucleotide synthesis via the regulation of E2F transcription factors which control the expression of *de novo* nucleotide synthesis genes (Vannucchi et al., 2000; Vernier et al., 2011). Given the inability of nucleotides or nucleosides to rescue IFN-induced cell-cycle alterations, it is possible that additional factors not accounted for here contribute to this phenotype. Moreover, several IFN-regulated metabolic genes possess secondary functions; in addition to its metabolic role, SAMHD1 mediates DNA repair by functioning as a CtIP scaffold (Daddacha et al., 2017). Thus, SAMHD1 induction by type I IFN signaling may reduce dNTP abundance while simultaneously facilitating DNA repair. Our findings suggest that IFN-induced replication stress is the consequence of alterations in multiple IFN-regulated genes. Additionally, we focused our investigation on human cells, as significant differences between the nucleotide metabolism of humans and mice have been noted (Kim et al., 2016).

This study begins to define the functional interplay between cytokine signaling, nucleotide metabolism, and replication stress in PDAC. Furthermore, this work provides the rationale for further investigations of emerging IFN-stimulating therapies as companions for ATR inhibitors as well as for leveraging IFN response transcriptional signatures as patient stratification biomarkers for ATR inhibitor-anchored therapeutic regimens currently under clinical evaluation in multiple malignancies.

STAR★METHODS

RESOURCE AVAILABILITY

Lead contact—Reagent or resource requests should be submitted to and will be fulfilled by the lead contact, Caius G. Radu (cradu@mednet.ucla.edu).

Materials availability—All unique/stable reagents generated in this study are available from the Lead Contact with a completed Materials Transfer Agreement.

Data and code availability—Results from nLC-MS/MS proteomics analysis of SUIT2 cells treated ±100 U/mL IFNβ for 24 hours related to Figure 2 are included as Table S1. Results from nLC-MS/MS phosphoproteomics analysis of SUIT2 cells treated ±100 U/mL IFNβ for 24 hours related to Figure 2 are included as Table S2. Full kinase inhibitor library

phenotypic screen results of SUIT2 cells treated ±100 U/mL IFNβ alongside a library of 430 protein kinase inhibitors for 72 hours related to Figure 2 are included as Table S3.

This paper does not report original code.

Any additional information required to reanalyze the data reported in this work paper is available from the Lead Contact upon request.

EXPERIMENTAL MODEL AND SUBJECT DETAIL

Cell culture—Cell culture was performed as previously described (Liang et al., 2021). All cancer cell cultures were maintained between passages 3 and 20 and maintained in antibiotic free Dulbecco's Modified Eagle's Medium (DMEM) +10% fetal bovine serum (FBS) at 37°C in 5% CO_2. Cell cultures were routinely monitored for mycoplasma contamination using the PCR-based Venor Mycoplasma kit. PDAC cell lines were acquired either from a commercial vendor (ATCC, DSMZ) or from collaborators. Cell line identity was independently authenticated by PCR (Laragen, Culver City, CA). Immortalized human pancreatic cancer associated fibroblast cells were provided by Dr. Rosa F. Hwang at The University of Texas MD Anderson Cancer Center. A13A primary pancreas cancer cells were provided by the Iacabuzio-Donahue laboratory at Memorial Solan Kettering Cancer Center. HDPE cells were provided by the Tsao laboratory at the Ontario Cancer Institute.

Animal studies—Animal studies were performed as previously described (Liang et al., 2021). All animal studies were approved by the UCLA Animal Research Committee (ARC). For the development of subcutaneous tumor models, 6–8 week-old male NOD-Prkdc^{em26Cd52}; Il2rg^{em26Cd22}; NjuCrl coisogenic immunodeficient mice (NCG; CRL572; Charles River Laboratories) were injected subcutaneously on the flanks with 0.5×10^6 cells resuspended 1:1 in phosphate buffered saline (PBS):matrigel (50 μL: 50 μL). For orthotopic tumor studies SUIT2-TetR-STING^{R284M} cells were engineered to stably express firefly luciferase using lentiviral transduction and 3×10^4 cells were resuspended in 1:1 PBS:matrigel (15 μL:15 μL) and injected into pancreata of male NOD-Prkdc^{em26Cd52}Il2rg^{em26Cd22}/NjuCrl (NCG) mice. 7 days after inoculation, tumor radiance was measured by bioluminescence imaging (BLI) and this signal was used to randomize mice to treatment cohorts. For BLI, 5 minutes after intra-peritoneal injection of D-luciferin (50 μL at 50 μg/mL in 0.9% saline) mice were anesthetized under 2% isoflurane for 5 additional minutes and subsequently imaged using an IVIS Bioluminescence Imaging scanner (PerkinElmer). All BLI images were acquired using a 30 second exposure time and low binning. BLI quantification was performed using Living Image software (PerkinElmer) where a region of interest (ROI) was drawn over a whole tumor and the radiance (p/s) value was recorded. Subcutaneous tumor volumes were calculated by micro-computed tomography (μCT) analysis using a G8 PET/CT scanner (PerkinElmer). All tumor volume measurements were performed by trained technicians blinded to experimental conditions. For doxycycline treatment, mice were supplied with doxycycline hyclate supplemented diet intended to deliver a daily dose of 2–3 mg of doxycycline or a control diet. For treatment studies, AZD-6738 was formulated in 10% DMSO, 40% propylene glycol (PPG), 50% H_2O and administered at 25 mg/kg p.o. b.i.d. in a volume of 100 μL/20 g mouse.

METHOD DETAILS

Drug preparation for *in vitro* studies—Drugs for *in vitro* studies were prepared as previously described (Liang et al., 2021). Drug stocks were prepared in neat dimethylsulfoxide (DMSO) or H_2O, stored at $-80°C$, and diluted fresh in cell culture media for experiments. The non-hydrolyzable bisphosphorothioate $2^{'}–3^{'}$-cGAMP analog (cGAMP-PS) and interferon-stimulatory DNA (ISD) were complexed with Lipofectamine 3000 before treatment.

Analysis of PDAC TCGA sample gene expression—The Cancer Genome Atlas (TCGA) pancreatic ductal adenocarcinoma gene expression data (Cancer Genome Atlas Research Network, 2017) were filtered to exclude neuroendocrine and low-purity tumors and to include only tumors that were sub-typed consistently by previously set definitions (Bailey et al., 2016; Collisson et al., 2011; Moffitt et al., 2015). Basal-like like tumors were only included if they were defined as basal-like by Moffitt et al., quasimesenchymal by Collisson et al., and squamous by Bailey et al. Classical-subtype tumors were only included if they were defined as classical by Moffitt et al., classical by Collisson et al., and pancreatic progenitor by Bailey et al. which gave 11 basal-like and 30 classical tumors. Filtered tumors were clustered by expression of a previously defined 24 gene interferon response signature (Figure 1A) (Doherty et al., 2017) or with a expanded list of 104 genes which including the MSigDB Hallmark gene set for INTERFERON ALPHA RESPONSE (Figure S1A). Expression data were z-scored for visualization.

Immunohistochemistry (IHC)—IHC analysis was performed as previously described (Moore et al., 2021). Formalin-fixed, paraffin-embedded tumor samples were incubated at $60°C$ for 1 hour, deparaffinized in xylene, and rehydrated with graded alcohol washes. Slides were then boiled in 0.01 M sodium citrate buffer for 15 minutes followed by quenching of endogenous peroxidase with 3% hydrogen peroxide. After 1 hour of blocking with 5% donkey serum at room temperature, primary antibodies (diluted 1:100) were added and slides were incubated overnight at $4°C$. Biotin-conjugated anti-rabbit secondary antibody (1:500) was added, slides were incubated for 1 h at $4°C$ and signal was developed using the Elite Vectastain ABC kit. IHC scoring was performed by a blinded pathologist with expertise in pancreatic cancer. Specimens were assigned a semiquantitative histoscore (0–300), which was the product of staining intensity (0 = negative, 1 = weak, 2 = moderate, 3 = strong) and percentage (0–100) of tumor cells staining at that intensity. Antibodies are reported in key resources table.

IHC analysis of PDAC tissue microarray (TMA) patient samples—All studies involving patient specimens were performed with appropriate institutional review board approvals. The UCLA PDAC TMA has been previously described and was generated from surgical resections performed on treatment naıve, AJCC stage I/II PDAC at UCLA (n = 138) (Manuyakorn et al., 2010). STING (TMEM173) levels were evaluated across three representative 1.0 mm cores per tumor using a semiquantitative histoscore (0–300), which is the product of staining intensity (0 = negative, 1 = weak, 2 = moderate, 3 = strong) and percentage (0–100) of tumor cells staining at that intensity. Values presented represent average histoscore. Scoring was performed blinded.

Protein kinase inhibitor phenotypic high throughput screen—Phenotypic screening was performed as previously described (Abt et al., 2020). A library of 430 protein kinase inhibitors was arrayed in polypropylene 384-well plates at 2003 concentrations covering a 7-point concentration range (corresponding to 13 concentrations: 5 μM, 1.65 μM, 550 μM, 185 μM, 61.5 nM, 20.6 nM, 6.85 nM). 25 μL per well of growth media (DMEM +10% FBS) ± 200 U/mL IFNβ (for a final concentration of 100 U/mL) was plated in opaque-white 384-well plates using a BioTek multidrop liquid handler. Protein kinase inhibitors were added by 250 nL pin-tool transfer (BioMek FX, Beckman-Coulter) and inhibitor/media mixtures were incubated at room temperature for 30 minutes. 25 μL of a 40,000 cells/mL suspension of SUIT2 cells (for 1000 cells/well) was subsequently added to each well. After 72 hours of incubation at 37°C 5% CO_2, 50 μL of CellTiter-Glo reagent diluted 1:4 in dH_2O was added to each well and luminescence was measured using a Wallac plate reader (Perkin Elmer). Each condition was assayed in duplicate (n = 2). Percent of control proliferation values for each condition were calculated by normalizing experimental wells to plate 0.5% DMSO controls and averaging replicate values. Composite synergy scores for each test compound were defined as the sum of the Synergy Score (% proliferation inhibition observed - % proliferation inhibition expected; calculated using the Excess over Bliss Additivity method) between IFNβ and individual protein kinase inhibitor concentrations across the 7-point concentration range (Greco et al., 1995). Z' factor scores for individual assay plates were calculated using eight positive and eight negative control wells on each plate. All plates gave a Z' factor >0.5 (Zhang et al., 1999).

Tumor tissue homogenization—Fragments from resected tumors were weighed (30–80 mg), transferred to Omni Hard Tissue homogenization vials, snap-frozen in liquid nitrogen and stored at −80°C before processing. 7.5 μL/mg tissue of tissue lysis buffer (50 mM ammonium bicarbonate pH 7.2, 0.5% sodium deoxycholate, 12 mM sodium laurel sarcosine; supplemented with protease and phosphatase inhibitors cocktails) was added and samples were homogenized using an Omni Bead Ruptor Elite (8 cycles of: 15 seconds on, 30 seconds off, speed 8) chilled to 4°C. Tissue homogenates were cleared by centrifugation at 12,000 × g for 10 minutes at 4°C. Cleared lysates were normalized using the BCA method and prepared for immunoblot analysis.

Immunoblot analysis—Immunoblot analysis was performed as previously described (Liang et al., 2021). PBS-washed cell pellets obtained by trypsinization of cells and centrifugation at 450 × g for 5 minutes were resuspended in cold RIPA buffer supplemented with protease and phosphatase inhibitor cocktails. Sample protein content was determined using the BCA assay. Cell line and tumor samples were normalized by RIPA and 4× laemmli loading dye dilution, resolved on 4–12% Bis-Tris gels and electro-transferred to nitrocellulose membranes. After blocking with 5% nonfat milk in tris-buffered saline (TBS) + 0.1% tween-20 (TBS-T) for 30 minutes at room temperature, membranes were incubated overnight in primary antibodies diluted 1:1000 in 5% BSA in TBS-T at 4°C. Membranes were washed with TBS-T and incubated with horseradish peroxidase (HRP)-linked secondary antibodies prepared at a 1:2500 dilution in 5% nonfat dry milk/TBS-T for 1 hour at room temperature. HRP was activated by incubating membranes with a mixture of SuperSignal Pico and SuperSignal Femto enhanced chemiluminescence ECL reagents (33:1

ratio). Exposure of autoradiography film was used for detection. Antibodies are reported in key resources table.

Reverse Transcription-polymerase chain reaction (RT-PCR)—RT-PCR was performed as previously described (Liang et al., 2021). Total RNA was isolated from cell cultures using the NucleoSpin RNA kit and quantified by Nanodrop. Reverse transcription was performed using the High Capacity cDNA Reverse Transcription kit. Quantitative PCR was performed using EvaGreen qPCR Master Mix on the QuantStudio3 system. RNA expression values were normalized to housekeeping gene (ACTB) expression, calculated using the Ct method and reported as relative expression to vehicle control treated samples. Primer sequences are indicated in key resources table.

Enzyme-linked immunoassay (ELISA)—2.5×10^5 cells in 1 mL of DMEM +10% FBS were allowed to seed overnight in 24 well plates. $2^{'}–3^{'}$-cGAMP-PS was complexed with Lipofectamine 3000 in OptiMEM at a 1:1:2 cGAMP-PS:lipofectamine:OptiMEM ratio for transfection. For treatment, cells were washed with PBS, 400 μL of culture media was added to each well and 100 μL of complexed $2^{'}–3^{'}$-cGAMP-PS was added dropwise for a final concentration of 25 μg/mL. 6 or 24 hours after treatment, culture media was collected, centrifuged for 4 minutes at $450 \times g$ at 4°C and supernatant was analyzed by ELISA per manufacturers instructions.

Immuno-Fluorescence microscopy—SUIT2 cells were seeded on coverslips in 6-well plates and treated as indicated. Cells were fixed with 4% (w/v) paraformaldehyde in PBS for 15 minutes, permeabilized with 0.2% (v/v) Triton X-100, blocked with 3% (w/v) BSA in PBS for 30 minutes, and incubated with primary anti-ssDNA antibody diluted 1:100 in 1% BSA, 0.1% saponin in PBS overnight. Coverslips were washed with PBS then incubated with fluorochrome-conjugated secondary antibody diluted 1:250 in 1% BSA in PBS for 1 hour. Following washing, cells were stained with diamidino-2-phenylindole (DAPI), washed with PBS, mounted onto microscope slides and imaged using a NIKON Eclipse Ci-S fluorescence microscope.

Cell proliferation analysis—For anchorage-dependent Cell Titer Glo analysis, cells were seeded at 1×10^3 cells per well in 50 μL of DMEM + 10% FBS in white opaque 384-well plates and treated as described. After 72 hours, 50 μL of 3D Cell Titer Glo reagent (diluted 1:5 in PBS) was added to each well, plates incubated at room temperature for 5 minutes and luminescence was measured using a Synergy H1 microplate luminescence reader.

For live-cell imaging cells were seeded at 5×10^3 cells per 100 μL per well in ultra-low attachment U-bottom 96-well plates (for anchorage- independent culture) or flat bottom 96-well plates (for anchorage- dependent culture). After 24–72 hours, treatments were added to a final volume of 200 μL and cell proliferation was tracked using the IncuCyte Zoom live-cell imaging system. Images were acquired at 3 hour intervals over the indicated time period. Sphere area analysis was applied to quantify proliferation for anchorage-independent cultures. Percent confluence analysis was applied to quantify proliferation for anchorage-dependent cultures.

Flow cytometry—All flow cytometry data were acquired on a five-laser LSRII, and analyzed using FlowJo software.

AnnexinV/PI—Following treatment, adherent PDAC cells were trypsinized, washed twice with PBS and incubated with AnnexinV-FITC and propidium iodide diluted in 1× annexin binding buffer per manufacturers instructions.

Propidium iodide cell cycle analysis—Following treatment, adherent PDAC cells were trypsinized, washed twice with PBS and suspended in 500 μL of cell cycle staining solution (100 μg/mL propidium iodide, 20 μg/mL ribonuclease A, 1 mg/mL sodium citrate, 0.3% Triton-X 100 in dH₂O).

pH2A.X-S139—Following treatment, adherent PDAC were trypsinized, washed twice with PBS, fixed and permeabilized with cytofix/cytoperm for 15 minutes on ice, and stained with FITC-conjugated anti-pH2A.X-S139 antibody (prepared at a 1:800 dilution in perm/wash) for 20 minutes at room temperature shielded from light. Cells were subsequently washed twice with PBS and stained with 0.5 mL of DAPI (250 ng/mL in PBS) before analysis.

EdU pulse—Cells were treated ± 100 U/mL IFNβ for 24 hours in 2 μL of DMEM +10% FBS in 6-well plates. Cells were subsequently pulsed with 10 μM EdU for 2 hours before trypsinization. Isolated cells were fixed with 4% paraformaldehyde and permeabilized using saponin perm/wash reagent. Cells were then stained with azide-Alexa Fluor 488 by Click reaction according to manufacturers protocol. Cells were subsequently washed twice with PBS and stained with 0.5 μL of DAPI (250 ng/mL in PBS in 2% FBS) before analysis.

CRISPR/Cas9 knockout cell line generation—Gene knockout was performed as previously described (Liang et al., 2021). All guide RNA (gRNA)-encoding oligonucleotides were cloned into the LentiCrisprV2 vector. Lipofectamine 3000 was used to transfect PDAC cells with gRNA-specific LentiCrisprV2 vectors. Following puromycin selection, cells were singly cloned and gene knockout was confirmed by genomic DNA PCR/TIDE in/del analysis of Sanger sequencing results. Gene knockout was additionally validated using immunoblot analysis.

Generation of doxycycline-inducible STING^R284M models—The generation of SUIT2-TetR-STING^R284M cells was previously described (Moore et al., 2021). A STING^R284M encoding gene fragment was ligated into the pENTR-D/TOPO entry vector. Resulting constructs were recombined into pLenti-CMV/TO-GFP/PURO using Gateway LR Clonase II. For virus production lentivirval vectors and packaging plasmids (psPAX2, pMD2G) at a 2:1:1 ratio were transfected into FT293 cells using polyethylenimine. Transduced cells were selected in puromycin for 1 week. In this model STING^R284M expression is regulated by the doxycycline responsive Tet repressor (TetR) protein expressed from the pLenti3/EF/GW/IVS-Kozak-TetR-P2A-Bsd vector.

Metabolite extraction for liquid chromatography mass spectrometry (LC-MS) metabolomics analysis—0.75×10^6 SUIT2, YAPC and PANC1 cells were plated in 6-well plates (n = 6/condition) in 2 μL of DMEM + 10% FBS and seeded overnight. For

treatment, media was replaced ±100 U/mL IFNβ. After 24 hours, plates were transferred to ice, media was removed, wells were washed twice with 1 μL of 150 mM NH_4 acetate; and metabolite extraction buffer (80% MeOH in MiliQ-purified/LC-Pak treated H_2O + stable isotope-labeled nucleotide and amino acid internal standards: $[^{13}C,^{15}N]$amino acids (50 mM) and $[^{15}N]$r/dNTPs (25 mM), $[^{15}N]$r/dNMPs (5 mM), and $[^{15}N]$r/dNs (1 μM)) was added to each well for a final protein concentration of 0.4 μg/mL. Samples were incubated on ice for 10 minutes, scraped, transferred to 1.5 mL microcentrifuge tubes, vigorously vortexed and placed on dry ice until sample collection was completed. After incubation at −80°C for 30 minutes, samples were centrifuged at 12,000 × g for 15 minutes at 4°C to remove insoluble material. The protein-containing pellet was resuspended in 500 μL of tissue lysis buffer (50 mM ammonium bicarbonate pH 7.2, 0.5% sodium deoxycholate, 12 mM sodium laurel sarcosine), incubated at 4°C for 15 minutes, sonicated and evaluated using the BCA method to determine protein content. In parallel, MeOH-extracted supernatants were transferred to 1.5 mL microcentrifuge tubes and dried in a speed-vac overnight. Metabolite pellets were reconstituted in 60% acetonitrile in MiliQ-purified/LC-Pak treated H_2O at 5 μL for each 100 μL of metabolite extraction buffer dried (equivalent to 8 μg/μL of extracted protein). Reconstituted metabolite samples were vortexed, transferred to HPLC injector vials and injected directly onto a Waters Acquity UPLC BEH Amide Column (130A, 1.7 μm, 3 mm × 150 mm) and effluent was directed to a LTQ-Orbitrap XL mass spectrometer.

Media metabolite extraction, DNA isolation/hydrolysis and targeted mass spectrometry (LC-MS/MS-MRM) analysis—For stable isotope tracing experiments, 0.75×10^6 cells in 2 mL of DMEM + 10% FBS were seeded overnight in 6-well plates. For treatment, cells were washed twice with PBS and media was replaced with glucose-free DMEM +10% dialyzed FBS +1 g/L $[^{13}C_6]$ glucose ±100 U/mL IFNβ. Media and DNA analysis were performed on samples obtained from a single well. Intracellular metabolite analysis was performed on samples plated and treated in parallel.

For analysis of media nucleosides, a a modified version of previously reported method was applied (Liang et al., 2021). At experimental endpoints, media was collected in a 1.5 mL microcentrifuge tube, centrifuged at 450 × g for 5 minutes at 4°C and the supernatant was stored at −80°C. For metabolite extraction, 20 μL of supernatant was mixed with 80 μL of 100% MeOH containing stable isotope-labeled nucleoside internal standards (0.5 μM $[^{15}N]$r/dNs). MeOH-extracted samples were incubated at −80°C for 24 hours before transfer to a HPLC injector vial and LC-MS/MS-MRM analysis.

For analysis of stable isotope labeling of nucleosides in DNA, a modified version of a previously reported method was applied (Le et al., 2017). Cells were harvested by trypsinization, genomic DNA was extracted using the Quick-gDNA MiniPrep kit, and DNA was hydrolyzed to nucleosides using the DNA Degradase Plus kit following manufacturer-supplied instructions. In the final step of purification, 50 μL of H_2O was used to elute DNA into 1.5 μL microcentrifuge tubes. 50 μL of a DNA nuclease solution (10× buffer/DNA Degradase Plus/H_2O; 2.5/1/1.5) was added to 20 μL of eluted genomic DNA in an HPLC injector vial. Samples were incubated overnight at 37°C before analysis.

Liquid Chromatography-Mass Spectrometry (LC-MS/MS) of hydrolyzed DNA and media was performed as previously described (Le et al., 2017). 5 μL of sample was injected onto a porous graphitic carbon column (Thermo Fisher Scientific Hypercarb, 100×2.1 mm, 5 μm particle size) equilibrated in solvent A (0.1% formic acid in MiliQ-purified/LC-Pak treated H_2O) and eluted (700 μL/min) with an increasing concentration of solvent B (0.1% formic acid in acetonitrile) using min/%B/flow rates (μL/min) as follows: 0/2/700, 3/80/700, 4/80/700, 4.5/2/700, 7/2/700. The effluent from the column was directed to a Agilent Jet Stream ion source connected to a Agilent 6460 triple quadrupole mass spectrometer operating in the multiple reaction monitoring (MRM) mode using previously optimized settings. The peak areas for each nucleoside (precursor $\rightarrow$ fragment ion transitions) at predetermined retention times were recorded using Agilent MassHunter software. Peak areas were normalized to nucleoside internal standard signals. An external standard curve was applied to determine media nucleoside concentrations. Experimental and standard samples were processed together to minimize variation.

Intracellular nucleotide extraction and LC-MS/MS-MRM analysis—For intracellular nucleotide analysis, a modified version of a previously reported method was utilized (Le et al., 2017). 0.75×10^6 cells in 2 mL of DMEM +10% FBS were seeded overnight in 6-well plates. For treatment, media was replaced with glucose-free DMEM +10% dialyzed FBS +1 g/L [$^{13}C_6$]glucose ±100 U/mL IFNβ. After 24 hours, metabolites were extracted and dried as described for LC-MS analysis. Dried metabolite pellets were reconstituted in MiliQ-purified/LC-Pak treated H_2Oat 5 μL for each 100 μL of metabolite extraction buffer dried (samples were concentrated 203). Reconstituted samples were vortexed and transferred to HPLC injector vials. 5 μL was injected directly onto a Hypercarb column (100×2.1 mm, 5 mm particle size) equilibrated in solvent A (5 mM hexylamine and 0.5% diethylamine in MiliQ-purified/LC-Pak treated H_2O, pH adjusted to 10.0 using glacial acetic acid) and eluted (200 μL/min) with an increasing concentration of solvent B (100% acetonitrile) at the following min/%B/flow rates (μL/min): 0/5/200, 15/60/200, 15.5/60/600, 18/5/600, 20.5/5/200, 23/5/200. The effluent from the column was directed to a Agilent Jet Stream ion source connected to a Agilent 6460 triple quadrupole mass spectrometer operating in the MRM mode using previously optimized settings. The peak areas for each nucleotide (precursor/fragment ion transitions) at predetermined retention times were recorded using Agilent MassHunter software and were normalized to nucleotide internal standards. An external standard curve was applied to determine nucleotide concentrations which were normalized to the protein content of individual samples.

Proteomics and phosphoproteomics—A modified version of a previously described proteomics and phosphoproteomics sample processing, data acquisition and analysis workflow was applied (Stuparu et al., 2021).

Protein extraction, digestion, labeling and pooling—SUIT2 cells were treated as indicated and washed twice with ice cold PBS and lysed in fresh lysis buffer (50 mM triethylammonium bicarbonate, pH 8.5, 0.5% sodium deoxycholate, 12 mM sodium lauroyl sarcosine, MS-SAFE protease inhibitor cocktail (Sigma-Aldrich) and phosphatase inhibitor cocktail containing 10 mM sodium pyrophosphate, 50 mM sodium fluoride, 1 mM

sodium orthovanadate, and 50 mM beta-glycerophosphate). Protein lysates were sonicated for 10 minutes, 30 seconds on 30 seconds off, at 4°C using Bioruptor Pico (Diagenode) followed by heating at 95°C for 5 minutes. The protein concentration of lysates were quantified by the BCA protein assay and 1 mg of total protein from each sample was carried through subsequent sample preparation. Protein disulfides were reduced with 5 mM dithiolthreitol (final concentration) for 30 minutes at 37°C followed by alkylation with 10 mM chloroacetamide (final concentration) for 30 minutes at room temperature in the dark. Excess alkylating agent was quenched by adding the same amount of dithioltheritol as the previous step and incubating for 5 minutes at room temperature. Each sample was then diluted 1:5 using 50 mM triethylammonium bicarbonate, pH 8.5, containing 10 mg trypsin (Promega) and digested at 37°C for 4 hours. A second aliquot of 10 μg trypsin (Promega) was spiked into the samples and digested overnight at 37°C. The reaction was quenched and detergents extracted with 1:1 (v:v) ethyl acetate containing 1% trifluoroacetic acid. The samples were vortexed vigorously and centrifuged at 16,000xg for 5 minutes. The lower aqueous phase was transferred to new microcentrifuge tubes and dried by speedvac. The samples were reconstituted in 2% acetonitrile with 0.1% trifluoroacetic acid, desalted on Oasis HLB 10 mg cartridges (Waters), and dried by speedvac. Samples were resuspended in 200 mM EPPS, pH 8.5, and peptide concentration was obtained using Pierce Quantitative Colorimetric Peptide Assay (Thermo). 400 μg of peptides were labeled with 10-plex TMT reagents at 1:2 reagent:peptide concentration following the manufacturer's instruction, and dried by speedvac. Samples were reconstituted in 2% acetonitrile with 0.1% trifluoroacetic acid and 1 mg of total peptides from each sample were pooled and desalted using SDB StageTips as previously described (Rappsilber et al., 2007). 1 mg of total peptide from this pooled test sample was acquired via nanoLC-MS/MS on a QExactive Plus (Thermo) using a 3 hour gradient as later discussed. The raw data was processed using Proteome Discoverer v2.2 (Thermo) as later discussed. Each sample was normalized to the protein median fold change compared to the 126 m/z TMT channel and ~300 mg of each sample was pooled accordingly. The pooled peptide sample was desalted on an Oasis HLB 200 mg cartridge (Waters) and dried by speedvac.

Phosphopeptide enrichment by immobilized metal affinity chromatography
—Phosphopeptide enrichment was performed using Fe-IMAC as previously described (Swaney and Villén, 2016). Briefly, 3.3 mg of dried peptides were solubilized in 900 μL of phosphopeptide binding solution (80% acetonitrile and 0.1% TFA). 150 μL peptide aliquots were mixed with 165 μL of Fe-IMAC and incubated at room temperature for 30 minutes with shaking. The supernatant and all washes were collected, dried by speedvac, and desalted on an Oasis HLB 200 mg cartridge (Waters) to be later used for peptide fractionation and total protein quantification via nanoLC-MS/MS. The phosphopeptides were quickly eluted from beads with 100 μL of phosphopeptide elution solution (70% acetonitrile and 1% ammonium hydroxide), passed through C8 StageTip and acidified with 30 μL of 10% formic acid. The phosphopeptide eluents were dried by speedvac and desalted using SDB StageTips.

Offline basic pH reverse phase liquid chromatography—The total phosphopeptide-enriched sample and 70 mg of the non-phosphopeptide sample were each solubilized in 3

μL of buffer A (10 mM ammonium bicarbonate, pH 10, and 2% acetonitrile) and separated on a Zorbax 300Extend-C18 column (3.5 mm particle size, 0.3 mm × 150 mm, Agilent) using an Agilent 1260 capillary pump and mWPS autosampler equipped with an 8 μL sample loop. 96 fractions were collected with a 60 minutes gradient from 5% to 60% buffer B (90% acetonitrile, 10 mM ammonium bicarbonate, pH 10, flow rate of 6 μL/min) into pre-deposited 20 μL of 5% formic acid. The samples were concatenated with an interval of 24 to form 24 final fractions (e.g. fractions 1, 25, 49, and 73 combined, fractions 2, 26, 50 and 74 combined, and so on). The concatenated fractions were desalted using SDB StageTips and dried by speedvac.

Acidic pH reverse phase liquid chromatography coupled with tandem MS—
The dried peptide fractions for whole proteome analysis were reconstituted in 11 μL of 2% acetonitrile and 0.15% formic acid. For phosphopeptide analysis, the dried peptide fractions were reconstituted in 6 uL of 2% acetonitrile and 0.15% formic acid. 5 μL of sample was loaded on a laser-pulled reverse phase column (150 mm × 20 cm, 1.8 mm C18 resin with 0.5 cm of 5 mm C4 resin at the laser-pulled end (Acutech Scientific)) interfaced with an Eksigent 2D nanoLC, Phoenix S&T dual column source, and QExactive Plus MS (Thermo). Peptides were eluted using 5–40% buffer B gradient in 3 hours (buffer A: 2% acetonitrile, 0.15% formic acid; buffer B: 98% acetonitrile, 0.15% formic acid, flow rate of 0.5 μL/min). The column was heated at 60C by a butterfly portfolio heater (Phoenix S&T) to reduce backpressure. The mass spectrometer was operated in data-dependent mode with a survey scan from 350–1500 m/z (70,000 resolution, 3×10^6 AGC target and 100 ms maximal ion time) and 10 MS/MS scans with starting fixed m/z of 100 (35,000 resolution, 2×10^5 AGC target, 120 ms maximal ion time, 32 normalized collision energy, 1.2 m/z isolation window, and 30 second dynamic exclusion).

Identification and quantitation of peptides using Proteome Discoverer v 2.2
—The acquired MS/MS raw files were searched by the Sequest algorithm against a forward and reverse target/decoy database to estimate FDR. The target protein database was downloaded from the Uniprot human database (reference and additional sequences, 93,320 protein entries; downloaded in March 2018) and the decoy protein database was generated by reversing all target protein sequences. A contaminate protein database was included in the searches (244 protein entries; downloaded from MaxQuant 1.6.0.16). Spectra were searched with ±10 ppm for precursor ion and ±0.02 Da product ion mass tolerance, fully tryptic restriction, static mass shift for TMT-tagged N-terminus and lysine (+229.16293), carbamidomethylation to cysteine (+57.021), dynamic mass shift for oxidation of methionine (+15.995), deamidation of asparagine and glutamine (+0.984), acetylation of protein N-terminus (+42.011), phosphorylation of serine, threonine and tyrosine (+79.96633, only for phosphopeptide-enriched fractions), two maximal missed cleavages, three maximal modification sites, and the assignment of b and y ions. Putative peptide spectra matches were filtered by Percolator using 1% FDR. Post-translational modifications were site localized using ptmRS. TMT reporter ions were quantified using the most confident centroid with reporter ion mass tolerance at 20 ppm.

Proteome and phosphoproteome differential expression analysis—Differential expression events were defined by identifying proteins/phosphopeptides with between-treatment variance significantly larger than within-replicate variance using one-way ANOVA (analysis of variance). Significantly altered proteins and phosphopeptides were filtered using Benjamini-Hochberg (BH) procedure at 1% or 0.1% FDR respectively. All statistical analysis, principle component analysis, and unsupervised hierarchical clustering was performed using Python. Kinase substrate enrichment analysis (KSEA) was performed using the web tool (https://casecpb.shinyapps.io/ksea/). Briefly, the significantly-altered phosphopeptides were submitted and respective kinases were assigned using the PhosphositePlus database and NetworKin. Kinases were filtered with 5% FDR.

QUANTIFICATION AND STATISTICAL ANALYSIS

Data are presented as mean ± SD with number of biological replicates indicated in figure legends. Comparisons of two groups were evaluated using the unpaired two-tailed unpaired t test and P values less than 0.05 were considered significant. Comparisons of more than two groups were evaluated using one-way ANOVA followed by Bonferroni's multiple comparison test and P values less than 0.05/m, where m is the total number of possible comparisons, were considered significant.

Supplementary Material

Refer to Web version on PubMed Central for supplementary material.

ACKNOWLEDGMENTS

REFERENCES

Abt ER, Rosser EW, Durst MA, Lok V, Poddar S, Le TM, Cho A,Kim W, Wei L, Song J, et al. (2020). Metabolic modifier screen reveals secondary targets of protein kinase inhibitors within nucleotide metabolism. Cell Chem Biol.27, 197–205.e6. [PubMed: 31734178]

Alves-Fernandes DK, and Jasiulionis MG (2019). The role of SIRT1 on DNA damage response and epigenetic alterations in cancer. Int. J. Mol. Sci.20, E3153. [PubMed: 31261609]

Aran D, Lasry A, Zinger A, Biton M, Pikarsky E, Hellman A, Butte AJ, and Ben-Neriah Y. (2016). Widespread parainflammation in human cancer. Genome Biol.17, 145. [PubMed: 27386949]

Aune TM, and Pogue SL (1989). Inhibition of tumor cell growth by interferon-gamma is mediated by two distinct mechanisms dependent upon oxygen tension: induction of tryptophan degradation and depletion of intracellular nicotinamide adenine dinucleotide. J. Clin. Invest.84, 863–875. [PubMed: 2503544]

Bailey P, Chang DK, Nones K, Johns AL, Patch AM, Gingras MC, Miller DK, Christ AN, Bruxner TJ, Quinn MC, et al. (2016). Genomic analyses identify molecular subtypes of pancreatic cancer. Nature 531, 47–52. [PubMed: 26909576]

Baird JR, Friedman D, Cottam B, Dubensky TW, Kanne DB, Bambina S, Bahjat K, Crittenden MR, and Gough MJ (2016). Radiotherapy combined with novel STING-targeting oligonucleotides results in regression of established tumors. Cancer Res.76, 50–61. [PubMed: 26567136]

Balkwill F, Watling D, and Taylor-Papadimitriou J. (1978). Inhibition by lymphoblastoid interferon of growth of cells derived from the human breast. Int. J. Cancer 22, 258–265.

Barankiewicz J, Kaplinsky C, and Cohen A. (1986). Modification of ribonucleotide and deoxyribonucleotide metabolism in interferon-treated human Blymphoblastoid cells. J. Interferon Res.6, 717–727. [PubMed: 2437224]

Benci JL, Johnson LR, Choa R, Xu Y, Qiu J, Zhou Z, Xu B, Ye D, Nathanson KL, June CH, et al. (2019). Opposing functions of interferon coordinate adaptive and innate immune responses to cancer immune checkpoint blockade. Cell 178, 933–948.e14. [PubMed: 31398344]

Beyaert M, Starczewska E, Van Den Neste E, and Bontemps F. (2016).A crucial role for ATR in the regulation of deoxycytidine kinase activity. Biochem. Pharmacol.100, 40–50. [PubMed: 26620371]

Bianchi V, and Spychala J. (2003). Mammalian 5'-nucleotidases. J. Biol. Chem.278, 46195–46198. [PubMed: 12947102]

Brown JS, O'Carrigan B, Jackson SP, and Yap TA (2017). Targeting DNA repair in cancer: beyond PARP inhibitors. Cancer Discov.7, 20–37. [PubMed: 28003236]

Camici M, Garcia-Gil M, Pesi R, Allegrini S, and Tozzi MG (2019). Purine-metabolising enzymes and apoptosis in cancer. Cancers (Basel)11, E1354. [PubMed: 31547393]

Cancer Genome Atlas Research Network (2017). Integrated genomic characterization of pancreatic ductal adenocarcinoma. Cancer Cell 32, 185–203.e13. [PubMed: 28810144]

Cheon H, Holvey-Bates EG, Schoggins JW, Forster S, Hertzog P, Imanaka N, Rice CM, Jackson MW, Junk DJ, and Stark GR (2013). IFNb-dependent increases in STAT1, STAT2, and IRF9 mediate resistance to viruses and DNA damage. EMBO J.32, 2751–2763. [PubMed: 24065129]

Collisson EA, Sadanandam A, Olson P, Gibb WJ, Truitt M, Gu S, Cooc J, Weinkle J, Kim GE, Jakkula L, et al. (2011). Subtypes of pancreatic ductal adenocarcinoma and their differing responses to therapy. Nat. Med.17, 500–503. [PubMed: 21460848]

D'Angiolella V, Donato V, Forrester FM, Jeong YT, Pellacani C, Kudo Y, Saraf A, Florens L, Washburn MP, and Pagano M. (2012). Cyclin F-mediated degradation of ribonucleotide reductase M2 controls genome integrity and DNA repair. Cell 149, 1023–1034. [PubMed: 22632967]

Daddacha W, Koyen AE, Bastien AJ, Head PE, Dhere VR, Nabeta GN, Connolly EC, Werner E, Madden MZ, Daly MB, et al. (2017). SAMHD1 promotes DNA end resection to facilitate DNA repair by homologous recombination. Cell Rep.20, 1921–1935. [PubMed: 28834754]

Daemen A, Peterson D, Sahu N, McCord R, Du X, Liu B, Kowanetz K, Hong R, Moffat J, Gao M, et al. (2015). Metabolite profiling stratifies pancreatic ductal adenocarcinomas into subtypes with distinct sensitivities to metabolic inhibitors. Proc. Natl. Acad. Sci. U SA112, E4410–E4417. [PubMed: 26216984]

Dalin S, Sullivan MR, Lau AN, Grauman-Boss B, Mueller HS, Kreidl E, Fenoglio S, Luengo A, Lees JA, Vander Heiden MG, et al. (2019). Deoxycytidine release from pancreatic stellate cells promotes gemcitabine resistance. Cancer Res.79, 5723–5733. [PubMed: 31484670]

Doherty MR, Cheon H, Junk DJ, Vinayak S, Varadan V, Telli ML, Ford JM, Stark GR, and Jackson MW (2017). Interferon-beta represses cancer stem cell properties in triple-negative breast cancer. Proc. Natl. Acad. Sci. US A114, 13792–13797. [PubMed: 29229854]

El-Khamisy SF, Masutani M, Suzuki H, and Caldecott KW (2003).A requirement for PARP-1 for the assembly or stability of XRCC1 nuclear foci at sites of oxidative DNA damage. Nucleic Acids Res.31, 5526–5533. [PubMed: 14500814]

Elliott IA, Dann AM, Xu S, Kim SS, Abt ER, Kim W, Poddar S, Moore A, Zhou L, Williams JL, et al. (2019). Lysosome inhibition sensitizes pancreatic cancer to replication stress by aspartate depletion. Proc. Natl. Acad. Sci. U SA116, 6842–6847. [PubMed: 30894490]

Espinet E, Gu Z, Imbusch CD, Giese NA,Buscher M, Safavi M, Weisenburger S, Klein C, Vogel V, Falcone M, et al. (2021). Aggressive PDACs show hypomethylation of repetitive elements and the execution of an intrinsic IFN program linked to a ductal cell of origin. Cancer Discov.11, 638–659. [PubMed: 33060108]

Foote KM, Nissink JWM, McGuire T, Turner P, Guichard S, Yates JWT, Lau A, Blades K, Heathcote D, Odedra R, et al. (2018). Discovery and characterization of AZD6738, a potent inhibitor of

ataxia telangiectasia mutated and Rad3 related (ATR) kinase with application as an anticancer agent. J. Med. Chem.61, 9889–9907. [PubMed: 30346772]

Froeling FEM, Casolino R, Pea A, Biankin AV, and Chang DK (2021). Molecular subtyping and precision medicine for pancreatic cancer. J. Clin. Med.10, E149. [PubMed: 33406790]

Gizzi AS, Grove TL, Arnold JJ, Jose J, Jangra RK, Garforth SJ, Du Q, Cahill SM, Dulyaninova NG, Love JD, et al. (2018). A naturally occurring antiviral ribonucleotide encoded by the human genome. Nature 558, 610–614. [PubMed: 29925952]

Goldstone DC, Ennis-Adeniran V, Hedden JJ, Groom HC, Rice GI, Christodoulou E, Walker PA, Kelly G, Haire LF, Yap MW, et al. (2011). HIV-1 restriction factor SAMHD1 is a deoxynucleoside triphosphate triphosphohydrolase. Nature 480, 379–382. [PubMed: 22056990]

Greco WR, Bravo G, and Parsons JC (1995). The search for synergy:a critical review from a response surface perspective. Pharmacol. Rev.47, 331–385. [PubMed: 7568331]

Halbrook CJ, Pontious C, Kovalenko I, Lapienyte L, Dreyer S, Lee HJ, Thurston G, Zhang Y, Lazarus J, Sajjakulnukit P, et al. (2019). Macrophage-released pyrimidines inhibit gemcitabine therapy in pancreatic cancer. Cell Metab 29, 1390–1399.e6. [PubMed: 30827862]

Kamisawa T, Wood LD, Itoi T, and Takaori K. (2016). Pancreatic cancer. Lancet 388, 73–85. [PubMed: 26830752]

Kim W, Le TM, Wei L, Poddar S, Bazzy J, Wang X, Uong NT, Abt ER, Capri JR, Austin WR, et al. (2016). [18F]CFA as a clinically translatable probe for PET imaging of deoxycytidine kinase activity. Proc. Natl. Acad. Sci.U SA113, 4027–4032. [PubMed: 27035974]

Le TM, Poddar S, Capri JR, Abt ER, Kim W, Wei L, Uong NT, Cheng CM, Braas D, Nikanjam M, et al. (2017). ATR inhibition facilitates targeting of leukemia dependence on convergent nucleotide biosynthetic pathways. Nat. Commun.8, 241. [PubMed: 28808226]

Lecona E, and Fernandez-Capetillo O. (2018). Targeting ATR in cancer. Rev. Cancer 18, 586–595. [PubMed: 29899559]

Liang K, Abt ER, Le TM, Cho A, Dann AM, Cui J, Li L, Rashid K, Creech AL, Wei L, et al. (2021). STING-driven interferon signaling triggers metabolic alterations in pancreas cancer cells visualized by [^{18}F]FLT PET imaging. Proc. Natl. Acad. Sci. U SA118, e2105390118.

Liu H, Golji J, Brodeur LK, Chung FS, Chen JT, deBeaumont RS, Bullock CP, Jones MD, Kerr G, Li L, et al. (2019). Tumor-derived IFN triggers chronic pathway agonism and sensitivity to ADAR loss. Nat. Med.25, 95–102. [PubMed: 30559422]

Lopez-Contreras AJ, Specks J, Barlow JH, Ambrogio C, Desler C, Vikingsson S, Rodrigo-Perez S, Green H, Rasmussen LJ, Murga M, et al. (2015). Increased RRM2 gene dosage reduces fragile site breakage and prolongs survival of ATR mutant mice. Genes Dev.29, 690–695. [PubMed: 25838540]

Manuyakorn A, Paulus R, Farrell J, Dawson NA, Tze S, Cheung-Lau G, Hines OJ, Reber H, Seligson DB, Horvath S, et al. (2010). Cellular histone modification patterns predict prognosis and treatment response in resectable pancreatic adenocarcinoma: results from RTOG 9704. J. Clin. Oncol.28, 1358–1365. [PubMed: 20142597]

Moffitt RA, Marayati R, Flate EL, Volmar KE, Loeza SG, Hoadley KA, Rashid NU, Williams LA, Eaton SC, Chung AH, et al. (2015). Virtual microdissection identifies distinct tumor- and stroma-specific subtypes of pancreatic ductal adenocarcinoma. Nat. Genet.47, 1168–1178. [PubMed: 26343385]

Moore AM, Zhou L, Cui J, Li L, Wu N, Yu A, Poddar S, Liang K, Abt ER, Kim S, et al. (2021). NAD$^+$ depletion by type I interferon signaling sensitizes pancreatic cancer cells to NAMPT inhibition. Proc. Natl. Acad. Sci. U SA 118, e2012469118.

Motwani M, Pesiridis S, and Fitzgerald KA (2019). DNA sensing by the cGAS-STING pathway in health and disease. Nat. Rev. Genet.20, 657–674. [PubMed: 31358977]

Ouyang H, Mou L, Luk C, Liu N, Karaskova J, Squire J, and Tsao MS (2000). Immortal human pancreatic duct epithelial cell lines with near normal genotype and phenotype. Am. J. Pathol.157, 1623–1631. [PubMed: 11073822]

Parker BS, Rautela J, and Hertzog PJ (2016). Antitumour actions of interferons: implications for cancer therapy. Nat. Rev. Cancer 16, 131–144. [PubMed: 26911188]

Provance OK, and Lewis-Wambi J. (2019). Deciphering the role of interferon alpha signaling and microenvironment crosstalk in inflammatory breast cancer. Breast Cancer Res.21, 59. [PubMed: 31060575]

Rahib L, Smith BD, Aizenberg R, Rosenzweig AB, Fleshman JM, and Matrisian LM (2014). Projecting cancer incidence and deaths to 2030: the unexpected burden of thyroid, liver, and pancreas cancers in the United States. Cancer Res.74, 2913–2921. [PubMed: 24840647]

Ramanjulu JM, Pesiridis GS, Yang J, Concha N, Singhaus R, Zhang SY, Tran JL, Moore P, Lehmann S, Eberl HC, et al. (2018). Design of amidobenzimidazole STING receptor agonists with systemic activity. Nature 564, 439–443. [PubMed: 30405246]

Rappsilber J, Mann M, and Ishihama Y. (2007). Protocol for micro-purification, enrichment, pre-fractionation and storage of peptides for proteomics using StageTips. Nat. Protoc.2, 1896–1906. [PubMed: 17703201]

Rusinova I, Forster S, Yu S, Kannan A, Masse M, Cumming H, Chapman R, and Hertzog PJ (2013). Interferome v2.0: an updated database of annotated interferon-regulated genes. Nucleic Acids Res.41, D1040–D1046. [PubMed: 23203888]

Saldivar JC, Hamperl S, Bocek MJ, Chung M, Bass TE, Cisneros-Soberanis F, Samejima K, Xie L, Paulson JR, Earnshaw WC, et al. (2018). An intrinsic S/G_2 checkpoint enforced by ATR. Science 361, 806–810. [PubMed: 30139873]

Schwartz DM, Kanno Y, Villarino A, Ward M, Gadina M, and O'Shea JJ (2017). JAK inhibition as a therapeutic strategy for immune and inflammatory diseases. Nat. Rev. Drug Discov.17, 78.

Stuparu AD, Capri JR, Meyer CAL, Le TM, Evans-Axelsson SL, Current K, Lennox M, Mona CE, Fendler WP, Calais J, et al. (2021). Mechanisms of resistance to prostate-specific membrane antigen-targeted radioligand therapy in a mouse model of prostate cancer. J. Nucl. Med.62, 989–995. [PubMed: 33277393]

Swaney DL, and Villén J. (2016). Proteomic analysis of protein posttranslational modifications by mass spectrometry. Cold Spring Harb Protoc.2016, pdb.top077743.

Tang ED, and Wang CY (2015). Single amino acid change in STING leads to constitutive active signaling. PLoS One10, e0120090.

Tanji H, Ohto U, Shibata T, Taoka M, Yamauchi Y, Isobe T, Miyake K, and Shimizu T. (2015). Toll-like receptor 8 senses degradation products of single-stranded RNA. Nat. Struct. Mol. Biol.22, 109–115. [PubMed: 25599397]

Vannucchi S, Percario ZA, Chiantore MV, Matarrese P, Chelbi-Alix MK, Fagioli M, Pelicci PG, Malorni W, Fiorucci G, Romeo G, et al. (2000). Interferon-beta induces S phase slowing via up-regulated expression of PML in squamous carcinoma cells. Oncogene19, 5041–5053. [PubMed: 11042692]

Vanpouille-Box C, Demaria S, Formenti SC, and Galluzzi L. (2018). Cytosolic DNA sensing in organismal tumor control. Cancer Cell34, 361–378. [PubMed: 30216189]

Vendetti FP, Karukonda P, Clump DA, Teo T, Lalonde R, Nugent K, Ballew M, Kiesel BF, Beumer JH, Sarkar SN, et al. (2018). ATR kinase inhibitor AZD6738 potentiates CD8+ T cell-dependent antitumor activity following radiation. J. Clin. Invest.128, 3926–3940. [PubMed: 29952768]

Vernier M, Bourdeau V, Gaumont-Leclerc MF, Moiseeva O, Bégin V, Saad F, Mes-Masson AM, and Ferbeyre G. (2011). Regulation of E2Fs and senescence by PML nuclear bodies. Genes Dev.25, 41–50. [PubMed: 21205865]

Weichselbaum RR, Ishwaran H, Yoon T, Nuyten DS, Baker SW, Khodarev N, Su AW, Shaikh AY, Roach P, Kreike B, et al. (2008). An interferon-related gene signature for DNA damage resistance is a predictive marker for chemotherapy and radiation for breast cancer. Proc. Natl. Acad. Sci. U SA 105, 18490–18495. [PubMed: 19001271]

Wiredja DD, Koyuturk M, and Chance MR (2017). The KSEA App: a web€based tool for kinase activity inference from quantitative phosphoproteomics. Bioinformatics33, 3489–3491. [PubMed: 28655153]

Xia J, and Wishart DS (2010). MSEA: a web-based tool to identify biologically meaningful patterns in quantitative metabolomic data. Nucleic Acids Res.38, W71–W77. [PubMed: 20457745]

Xiao Y, Kwong M, Daemen A, Belvin M, Liang X, Hatzivassiliou G, and O'Brien T. (2016). Metabolic response to NAD depletion across cell lines is highly variable. PLoS One11, e0164166.

Zeman MK, and Cimprich KA (2014). Causes and consequences of replication stress. Nat. Cell Biol.16, 2–9. [PubMed: 24366029]

Zhang JH, Chung TD, and Oldenburg KR (1999). A simple statistical parameter for use in evaluation and validation of high throughput screening assays. J. Biomol. Screen4, 67–73. [PubMed: 10838414]

Zhang YW, Jones TL, Martin SE, Caplen NJ, and Pommier Y. (2009). Implication of checkpoint kinase-dependent up-regulation of ribonucleotide reductase R2 in DNA damage response. J. Biol. Chem.284, 18085–18095. [PubMed: 19416980]

Zhang Z, Ohto U, Shibata T, Krayukhina E, Taoka M, Yamauchi Y, Tanji H, Isobe T, Uchiyama S, Miyake K, et al. (2016). Structural analysis reveals that Toll-like receptor 7 is a dual receptor for guanosine and single-stranded RNA. Immunity45, 737–748. [PubMed: 27742543]

Highlights

- Interferon signaling biomarkers are enriched in a subset of PDAC tumors

- Phosphoproteomics and chemical genomics identify ATR as an interferon-induced codependency in PDAC cells

- Blocking ATR in combination with interferon signaling limits nucleotide pools

- ATR inhibitors restrict the growth of PDAC tumors in which interferon signaling is driven by STING
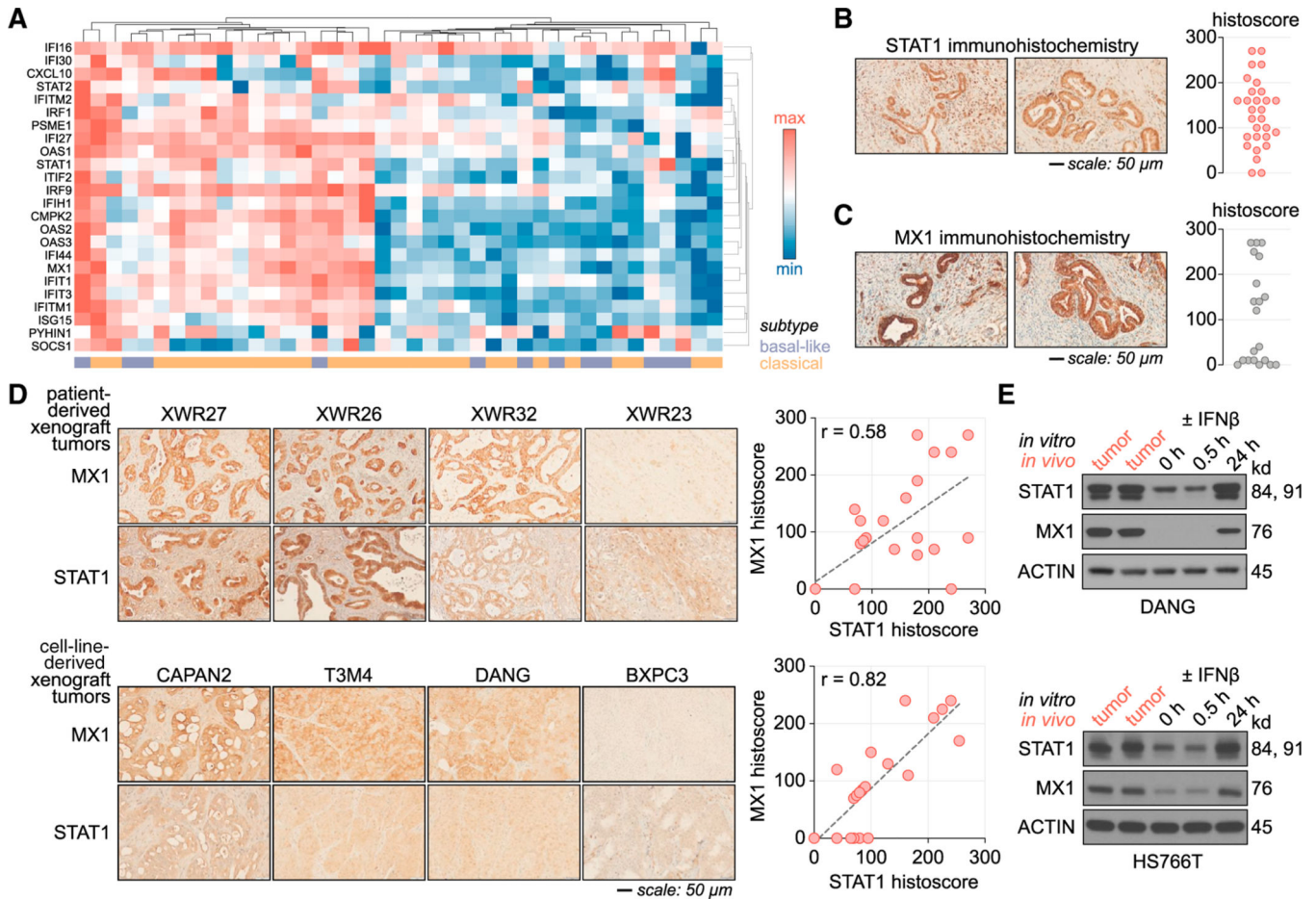
Figure 1. IFN signaling is enriched in a subset of PDAC tumors

(A) Analysis of an IFN response gene expression signature in the filtered TCGA PDAC dataset.

(B and C) Histoscores and representative immunohistochemistry (IHC) images of primary PDAC specimens probed for STAT1 (B) or MX1 (C; n = 26). Histoscores were calculated as a sum of the staining intensity (0, negative; 1, weak; 2, moderate; or 3, strong) multiplied by the percentage of tumor cells at that intensity (0–300 range).

(D) Representative STAT1 and MX1 IHC images and histoscores of PDAC-patient-derived (n = 33) and cell line (n = 17) xenograft tumors. Pearson correlation coefficient is indicated.

(E) Immunoblot analysis of DANG and HS766T cells treated ±100 U/mL IFNβ for the indicated timepoints *in vitro* and lysates prepared from DANG and HS766T subcutaneous tumors in NCG mice.
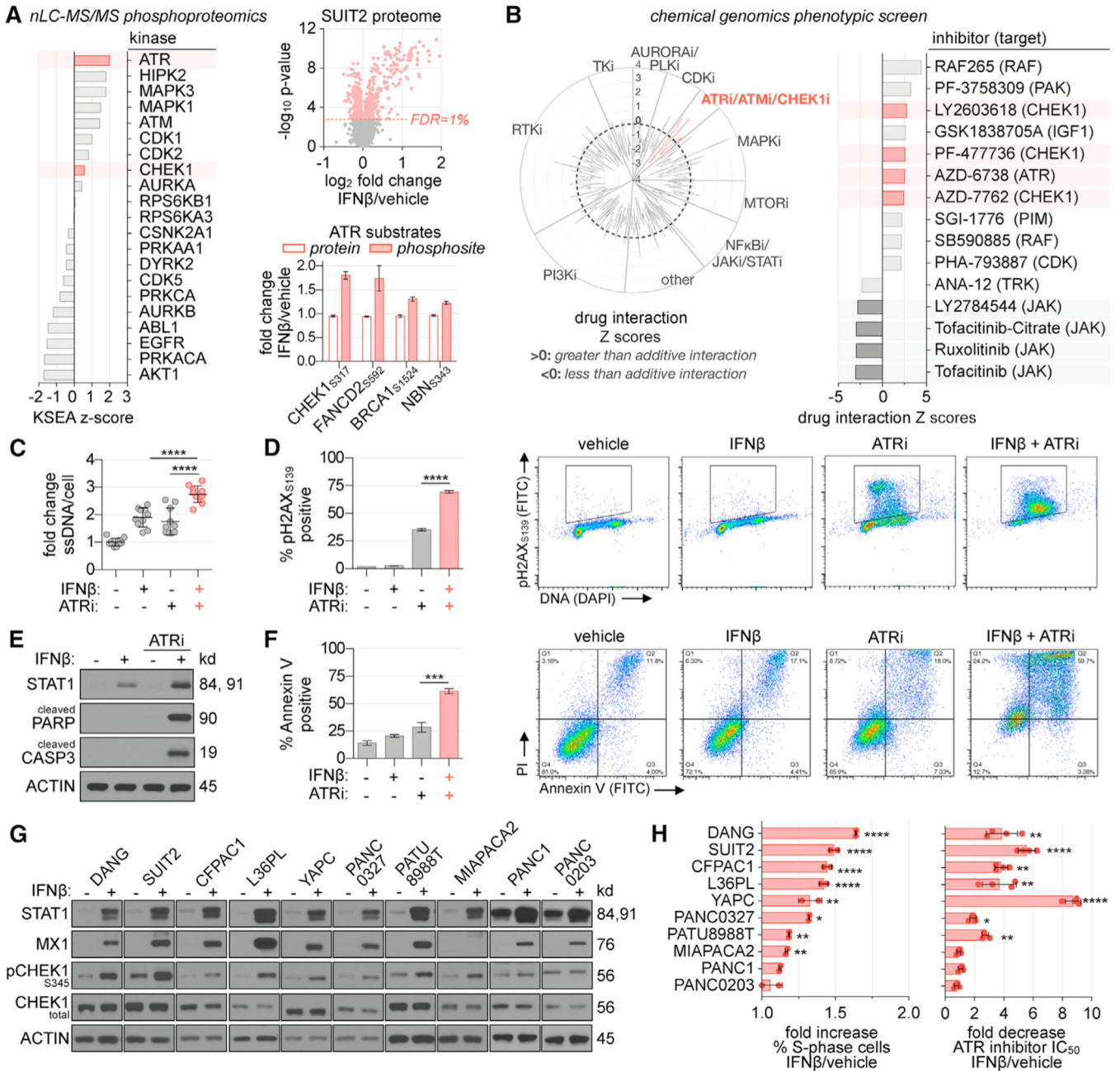
Figure 2. IFN triggers ATR activation and sensitizes PDAC cells to ATR inhibition
(A) nLC-MS/MS proteomics/phosphoproteomics analysis of SUIT2 cells treated ±100 U/mL IFNβ for 24 h. An FDR of 1% was applied to identify significantly altered proteins. An FDR of 0.1% was applied to identify significantly altered phosphopeptides. Kinase-substrate enrichment analysis (KSEA) of phospho-sites meeting the FDR cutoff was performed to infer alterations in protein kinase activity. A Z score >1 indicates activation and <1 indicates repression. ATR substrate phospho-sites meeting the 0.1% FDR cutoff and corresponding total protein levels are indicated (n = 5).

(B) High-throughput phenotypic screen evaluating the anti-proliferative effects of 430 protein kinase inhibitors using CellTiter-Glo. Compounds were tested at7-point dose response against SUIT2 cells treated ±100 U/mL IFNβ for 72 h (n = 2).

(C) Immunofluorescence microscopy analysis of ssDNA in SUIT2 cells treated ±100 U/mL IFNβ ±500 nM VE-822 (ATRi) for 24 h (mean ± SD; n = 10; one-way ANOVA corrected for multiple comparisons by Bonferroni adjustment).

(D) Flow cytometry analysis of pH2A.X$_{S139}$ levels in SUIT2 cells treated ±100 U/mL IFNβ ±500 nM ATRi for 48 h (mean ± SD; n = 2; one-way ANOVA corrected for multiple comparisons by Bonferroni adjustment).

(E) Immunoblot analysis of SUIT2 cells treated for 72 h ±100 U/mL IFNβ ±500 nM ATRi.

(F) AnnexinV/PI flow cytometry analysis of SUIT2 cells treated for 72 h ±100 U/mL IFNβ ±500 nM ATRi (mean ± SD; n = 2; one-way ANOVA corrected for multiple comparisons by Bonferroni adjustment).

(G) Immunoblot analysis of PDAC cell lines treated ±100 U/mL IFNβ for 24 h.

(H) Propidium iodide (PI) flow cytometry cell-cycle analysis of PDAC cells treated ±100 U/mL IFNβ, and CellTiter-Glo analysis of ATRi response in a panel of PDAC cell lines treated ±100 U/mL IFNβ for 72 h (mean ± SD; n = 4; unpaired t test). *p < 0.05; **p < 0.01; ***p < 0.001; ****p < 0.0001.
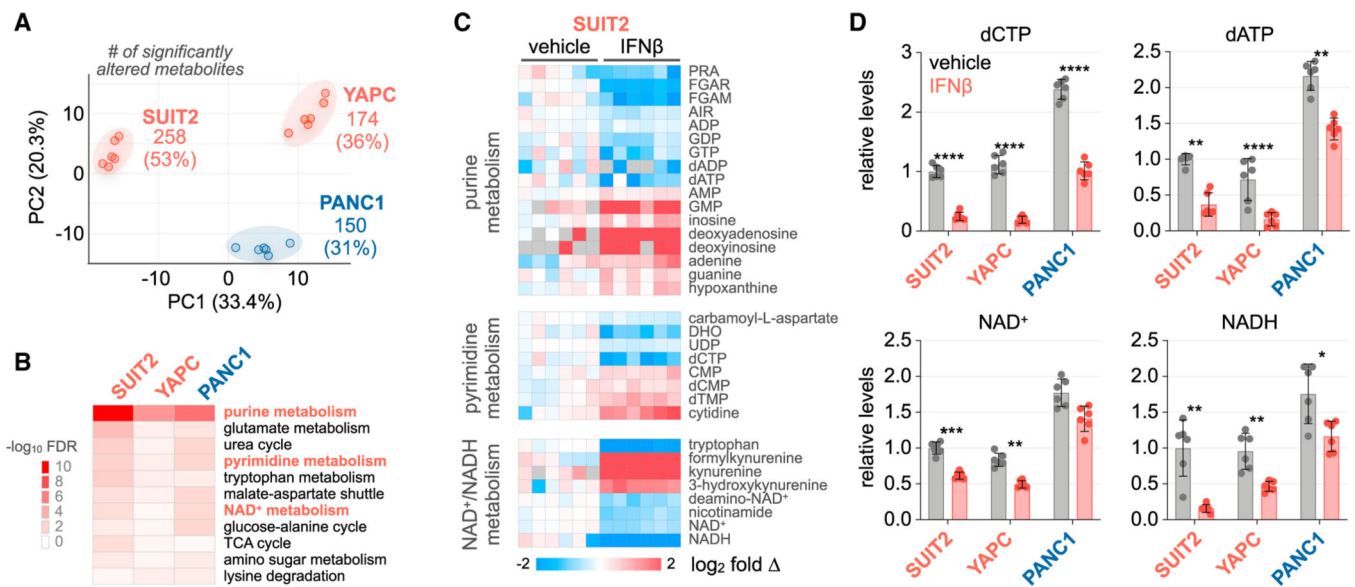
Figure 3. IFN alters nucleotide metabolism in PDAC cells

(A) Principal-component analysis (PCA) of fold changes in 485 metabolites measured by LC-MS in SUIT2, YAPC, and PANC1 cells treated ±100 U/mL IFNβ for 24 h (n = 6). Numbers and percentages of metabolites significantly altered by IFNβ treatment are indicated (FDR 10%).

(B) Metabolite set enrichment analysis (MSEA) of significantly altered metabolites in each cell line.

(C) Summary of IFN-induced alterations in nucleotide and NAD^+/NADH metabolism in SUIT2 cells.

(D) Relative levels of indicated metabolites in PDAC cell lines treated ±100 U/mL IFNβ for 24 h (mean ± SD, n = 6, unpaired t test). *p < 0.05; **p < 0.01; ***p < 0.001; ****p < 0.0001.

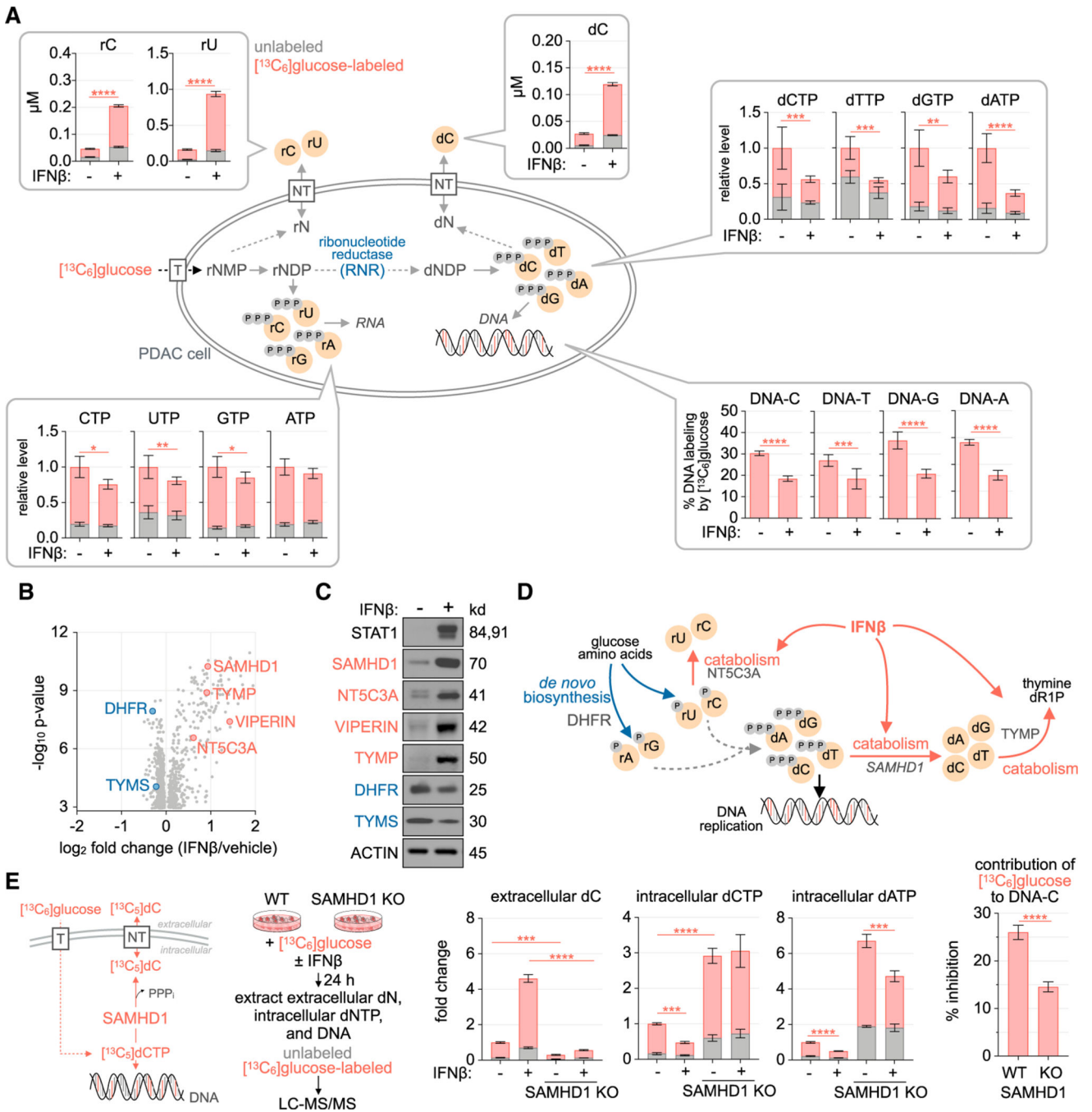**Figure 4. IFN restricts dNTP pools and enhances nucleoside efflux in PDAC cell lines**

(A) LC-MS/MS-MRM analysis of intracellular dNTP pools, DNA, and extracellular nucleosides in SUIT2 cells treated ±100 U/mL IFNβ for 24 h in media containing 1 g/L [$^{13}C_6$]glucose. Gray bars indicate unlabeled (M+0) fraction, and red bars indicate [$^{13}C_6$]glucose-labeled (M+5), newly synthesized fraction. DNA was hydrolyzed to nucleosides before analysis (mean ± SD; n = 6; unpaired t test; statistical analysis was performed only on [$^{13}C_6$]glucose-labeled fractions; NT: nucleoside transporter).

(B) Summary of nucleotide metabolism-related proteins significantly altered in SUIT2 cells following 24 h treatment ±100 U/mL IFNβ in the nLC-MS/MS proteomics dataset obtained in Figure 2A (1% FDR).

(C) Immunoblot analysis of SUIT2 cells treated ±100 U/mL IFNβ for 24 h.

(D) Schematic of the nucleotide metabolism-related processes impacted by IFN.

(E) Analysis of $[^{13}C_6]$glucose-labeled intracellular metabolite levels, extracellular media nucleoside levels, and contribution of $[^{13}C_6]$glucose to newly replicated DNA in SUIT2-wild type (WT) and SAMHD1-knockout (KO) measured using LC-MS/MS-MRM following treatment ±100 U/mL IFNβ for 24 h in media containing 1 g/L $[^{13}C_6]$glucose (mean ± SD; n = 3; one-way ANOVA corrected for multiple comparisons by Bonferroni adjustment). *p < 0.05; **p < 0.01; ***p < 0.001; ****p < 0.0001.
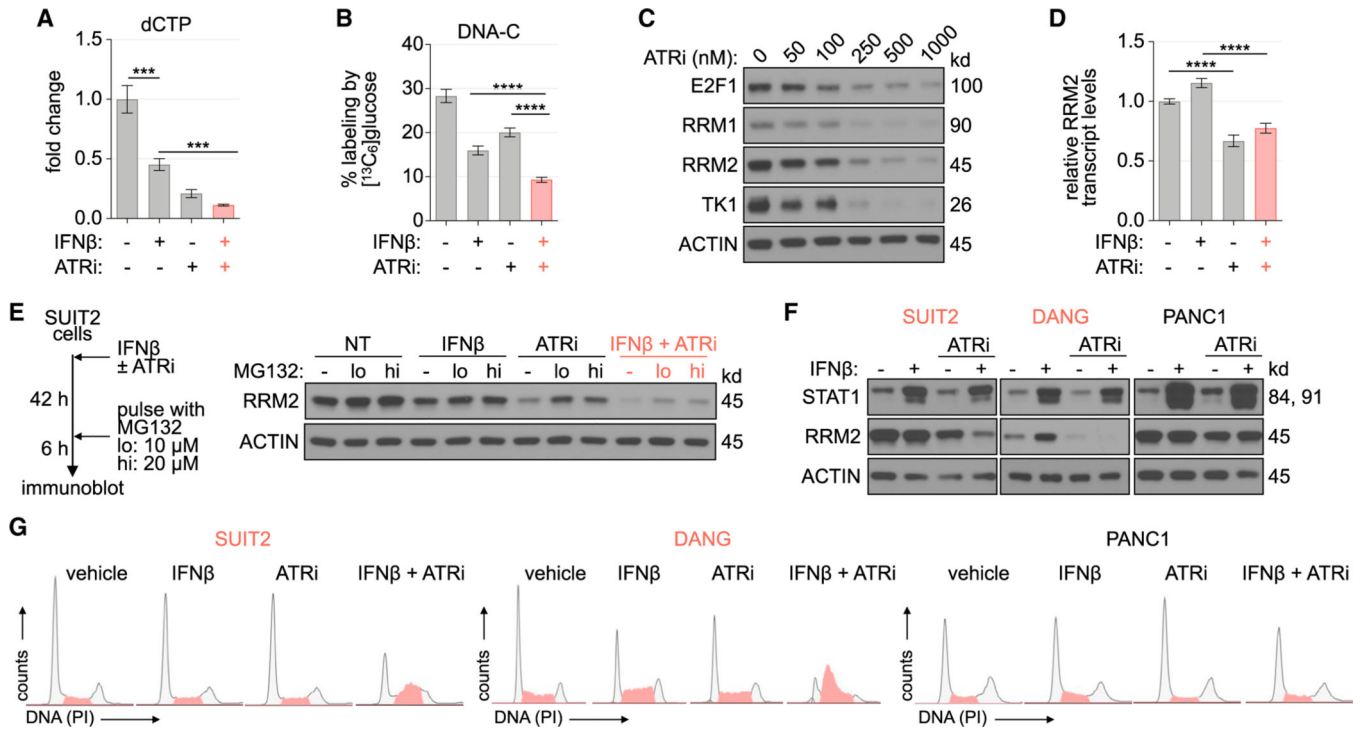
Figure 5. IFN and ATR inhibitors cooperatively restrict dNTP pools and S-phase progression

(A) LC-MS/MS analysis of dCTP pools in SUIT2 cells treated ±100 U/mL IFNβ±500 nM VE-822 (ATRi) for 24 h (mean ± SD; n = 3; one-way ANOVA corrected for multiple comparisons by Bonferroni adjustment).

(B) LC-MS/MS-MRM analysis of [$^{13}C_6$]glucose contribution to newly replicated DNA in SUIT2 cells treated ±100 U/mL IFNβ±500 nM ATRi for 24 h (mean ± SD; n = 3; one-way ANOVA corrected for multiple comparisons by Bonferroni adjustment).

(C) Immunoblot analysis of SUIT2 cells treated with indicated doses of ATRi in the presence of 100 U/mL IFNβ for 48 h.

(D) RT-PCR analysis of *RRM2* transcript levels in SUIT2 cells treated ±100 U/mL IFNβ±250 nM ATRi for 24 h (mean ± SD; n = 6; one-way ANOVA corrected for multiple comparisons by Bonferroni adjustment).

(E) Immunoblot analysis of SUIT2 cells treated as indicated in the presence of the proteasome inhibitor MG132.

(F) Immunoblot analysis of PDAC cells treated ±100 U/mL IFNβ±500 nM ATRi for 24 h.

(G) Flow cytometry cell-cycle analysis of PDAC cells treated ±100 U/mL IFNβ±500 nM ATRi for 24 h. ***p < 0.001; ****p < 0.0001.
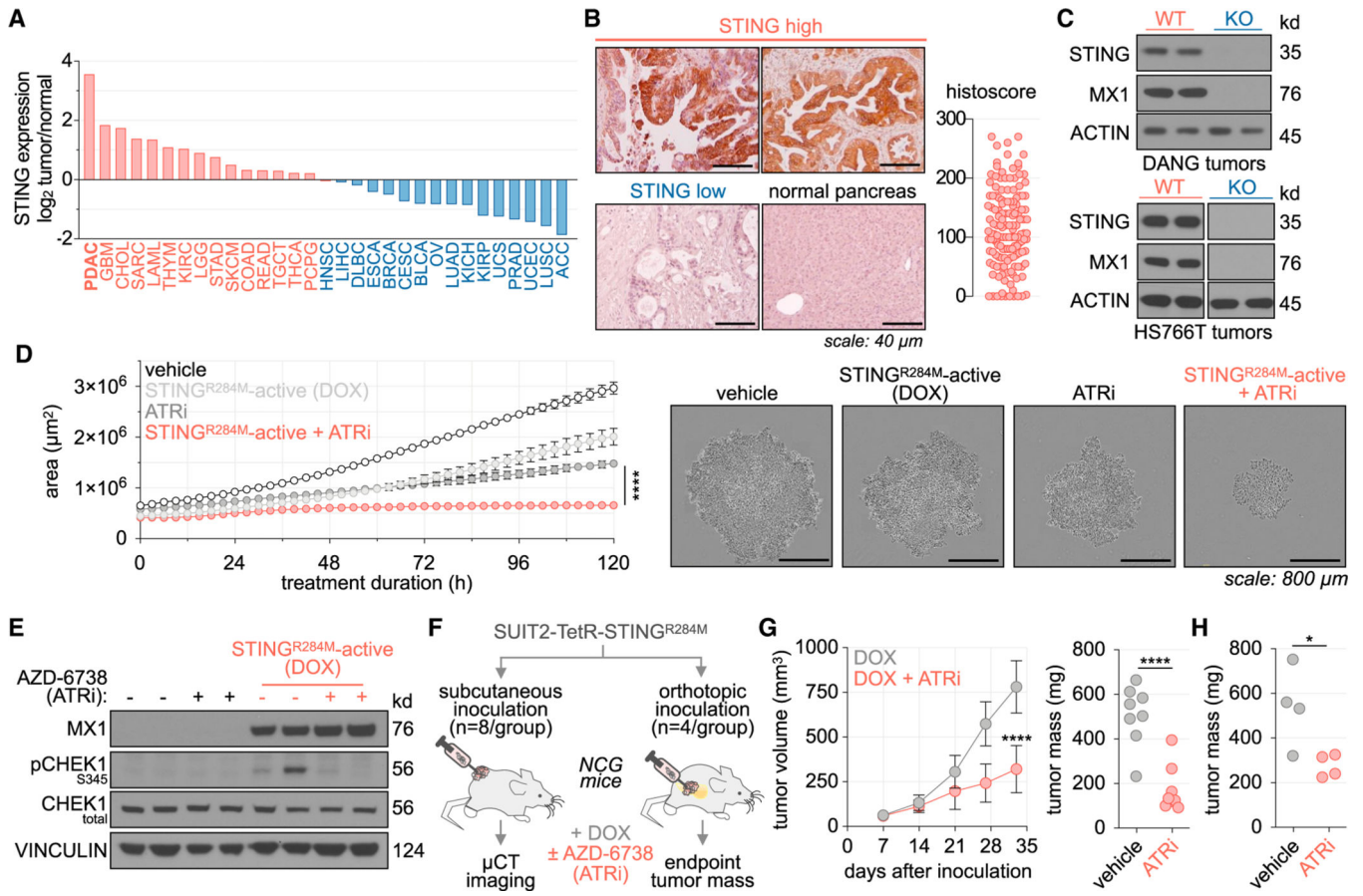
Figure 6. ATR inhibitors restrict the growth of PDAC tumors with STING-driven IFN signalling

(A) STING transcript levels across TCGA tumor datasets relative to GTEx organ-matched normal tissues.

(B) IHC analysis of STING expression in the UCLA PDAC tissue microarray (n = 138).

(C) Immunoblot analysis of protein lysates prepared from STING WT and CRISPR-Cas9 KO HS766T or DANG subcutaneous xenograft tumors.

(D) IncuCyte live-cell imaging analysis of SUIT2 TetR STING^{R284M} cells treated +50 ng/mL doxycycline (DOX) ± 500 nM VE-822 (ATR inhibitor [ATRi]) in anchorage-independent cultures (mean ± SD; n = 6; one-way ANOVA corrected for multiple comparisons by Bonferroni adjustment). Images are representative of respective experimental endpoints.

(E) Immunoblot analysis of SUIT2 tumors from mice treated ± DOX diet ± AZD-6738 (25 mg/kg b.i.d.) for 3 days.

(F) Experimental design to evaluate the impact of ATRi against PDAC tumors with active STING signaling.

(G and H) NCG mice were inoculated with subcutaneous (s.c.; G; n = 8) or orthotopic (H; n = 4) SUIT2 TetR STING^{R284M} tumors. Mice were fed a DOX-supplemented diet starting 7 days after tumor inoculation and treated ±25 mg/kg ATRi AZD-6738 b.i.d. for 26 days (unpaired t test; mean ± SD). Tumor volumes were measured using micro-computed tomography (μCT). Mass of excised tumor tissue is indicated. *p < 0.05; ****p < 0.0001.

KEY RESOURCES TABLE

REAGENT or RESOURCE	SOURCE	IDENTIFIER
Antibodies		
anti-STAT1 (IB/IHC), rabbit monoclonal	Cell Signaling Technology	Cat#14994; RRID:AB_2737027
anti-pSTAT1-Y701, rabbit monoclonal	Cell Signaling Technology	Cat#9167; RRID:AB_561284
anti-MX1 (IB/IHC), rabbit monoclonal	Cell Signaling Technology	Cat#37849; RRID:AB_2799122
anti-ACTIN, mouse monoclonal	Cell Signaling Technology	Cat#3700; RRID:AB_2242334
anti-VINCULIN, rabbit monoclonal	Cell Signaling Technology	Cat#13901; RRID:AB_2728768
anti-SAMHD1, rabbit polyclonal	Cell Signaling Technology	Cat#49158
anti-CHEK1, mouse monoclonal	Cell Signaling Technology	Cat#2360; RRID:AB_2080320
anti-pCHEK1-S345, rabbit monoclonal	Cell Signaling Technology	Cat#2348; RRID:AB_331212
anti-pH2AX-S139, rabbit monoclonal	Cell Signaling Technology	Cat#9718; RRID:AB_2118009
anti-TYMP, rabbit monoclonal	Cell Signaling Technology	Cat#4307; RRID:AB_10549070
anti-NT5C3A, rabbit polyclonal	Sigma-Aldrich	Cat#HPA010630; RRID:AB_2668319
anti-DHFR, mouse monoclonal	Novus Biologicals	Cat#MAB7934
anti-TYMS, rabbit monoclonal	Cell Signaling Technology	Cat#9045; RRID:AB_2797693
Ant-RSAD2 (VIPERIN)	Cell Signaling Technology	Cat#13996; RRID:AB_2734772
anti-CLEAVED PARP, rabbit monoclonal	Cell Signaling Technology	Cat#5625; RRID:AB_10699459
anti-CLEAVED CASPASE 3, rabbit polyclonal	Cell Signaling Technology	Cat#9662; RRID:AB_331439
anti-RRM2, rabbit monoclonal	Cell Signaling Technology	Cat# 65939
anti-E2F1, rabbit polyclonal	Cell Signaling Technology	Cat#3742; RRID:AB_2096936
anti-STING (TMEM173) (IB/IHC); rabbit monoclonal	Cell Signaling Technology	Cat#13647; RRID:AB_2732796
anti-pIRF3-S396; rabbit monoclonal	Cell Signaling Technology	Cat#37829; RRID:AB_2799121
anti-RABBIT IgG, HRP-LINKED, goat polyclonal	Cell Signaling Technology	Cat#7074; RRID:AB_2099233
anti-MOUSE IgG, HRP-LINKED, goat polyclonal	Cell Signaling Technology	Cat#7076; RRID:AB_330924
anti-RABBIT IgG BIOTIN, goat polyclonal	Jackson Laboratories	Cat#111–065-003; RRID:AB_2337959
anti-pH2AX-S139 FITC conjugate, mouse monoclonal	ThermoFisher Scientific	Cat#16–202-AMI
anti-ssDNA (F7.26), mouse monoclonal	Millipore	Cat#MAB3299; RRID:AB_11211010
Bacterial and virus strains		
Stbl3 chemically competent E. Coli	ThermoFisher Scientific	Cat#C737303
Biological samples		
Human peripheral blood mononuclear cells	UCLA	N/A
PDAC patient-derived xenograft (PDX) models	UCLA	N/A
Pancreatic cancer tissue microarray (deidentified)	Manuyakorn et al., 2010	N/A
Chemicals, peptides, and recombinant proteins		
DMEM	Corning	Cat#10–107-CV
Fetal bovine serum	Omega Scientific	Cat#FB-11
OptiMEM	ThermoFisher Scientific	Cat#31985–062

Antibodies

REAGENT or RESOURCE	SOURCE	IDENTIFIER
Lipofectamine 3000	ThermoFisher Scientific	L3000001
Human IFNβ	PBL Assay Science	Cat#11415–1
Human IFNγ	PBL Assay Science	Cat#11500–1
[$^{13}C_6$]glucose	Sigma-Aldrich	Cat#389374
VE-822	Cayman Chemicals	Cat#24198
AZD-6738	Cayman Chemicals	Cat#21035
LY2603618	Cayman Chemicals	Cat#20351
AZD-1775	Cayman Chemicals	Cat#21266
CHIR-124	Cayman Chemicals	Cat#16553
Ruxolitinib	Cayman Chemicals	Cat#11609
Doxycycline	Clontech	Cat#631311
2'3'-cGAM(PS)$_2$ (Rp/Sp)	Invivogen	Cat#tlrl-nacga2srs
Interferon stimulatory DNA (ISD)	Invivogen	Cat#tlrl-isdn
diABZI compound 3	Selleckchem	Cat#S8796
Lipofectamine 3000	ThermoFisher Scientific	Cat#L3000001
OptiMEM	ThermoFisher Scientific	Cat#31985–062
RIPA protein lysis buffer	Boston BioProducts	Cat#BP-115
Halt protease inhibitor cocktail	ThermoFisher Scientific	Cat#PI78430
Halt phosphatase inhibitor cocktail	ThermoFisher Scientific	Cat#PI78428
Laemmli loading dye	Boston BioProducts	Cat#BP-110R
4–12% Bis-tris protein gels	ThermoFisher Scientific	Cat#NP0336
Nitrocellulose membrane	ThermoFisher Scientific	Cat#88018
Nonfat dry milk	ThermoFisher Scientific	Cat#M-0841
Tris-buffered saline	ThermoFisher Scientific	Cat#50–751-7046
Tween-20	Sigma-Aldrich	Cat#P9416
Supersignal pico ECL reagent	ThermoFisher Scientific	Cat#34580
Supersignal femto ECL reagent	ThermoFisher Scientific	Cat#34095
Autoradiography film	Denville	Cat#E3012
DAPI	Invitrogen	Cat#D1306
CytoFIX/CytoPERM	BD Biosciences	Cat#554722
DNA degradase PLUS	Zymo	Cat#E2021
Hard tissue homogenizing vials	Omni International	Cat#19–628
Ultra-low attachment 96-well plates	ThermoFisher Scientific	Cat#07–201-680
Vectastain elite ABC kit	Vector Laboratories	Cat#PK-6100
Doxycycline supplemented rodent diet	Envigo	Cat#TD.120769
Control rodent diet	Envigo	Cat#TD.00588
Propylene glycol	Sigma-Aldrich	Cat#P4347
Matrigel	ThermoFisher Scientific	Cat#CB-40234
D-Luciferin	Goldbio	Cat#Luck
Ultra-low attachment 96-well plates	ThermoFisher Scientific	Cat#07–201-680

REAGENT or RESOURCE	SOURCE	IDENTIFIER
Antibodies		
Critical commercial assays		
AnnexinV-FITC apoptosis detection Kit	BD Biosciences	Cat#556547
BCA assay	ThermoFisher Scientific	Cat#23225
3D Cell Titer Glo	Promega	Cat#G9683
NucleoSpin RNA kit	Takara Bio	Cat#740955.25
MycoPlasma detection Kit	Sigma-Aldrich	Cat#MP0025
EvaGreen qPCR master mix	Lambda Biotech	Cat#MX-S
High-capacity cDNA reverse transcription kit	ThermoFisher Scientific	Cat#4368814
Quick RNA miniprep kit	Zymo	Cat#R1054
Quick genomic DNA miniprep kit	Zymo	Cat#D3021
Human IFNβ ELISA	PBL Assay Science	Cat#41410
EdU cell proliferation kit	ThermoFisher Scientific	Cat#C10337
Experimental models: Cell lines		
Human SUIT2 (male) cells	Accegen	Cat#ABC-TC1175; RRID:CVCL_3172
Human DANG (female) cells	DSMZ	Cat#ACC249; RRID:CVCL_0243
Human CFPAC1 (male) cells	ATCC	Cat#CRL1918; RRID:CVCL_1119
Human YAPC (male) cells	DSMZ	Cat#ACC382; RRID:CVCL_1794
Human PANC0327 (female) cells	ATCC	Cat#CRL2549; RRID:CVCL_1635
Human PATU8988T (female) cells	DSMZ	Cat#ACC162; RRID:CVCL_1847
Human MIAPACA2 (male) cells	ATCC	Cat#CRL1420; RRID:CVCL_0428
Human PANC1 (male) cells	ATCC	Cat#CRL1469; RRID:CVCL_0480
Human PANC0203 (female) cells	ATCC	Cat#CRL2553; RRID:CVCL_1633
Human HS766T (male) cells	ATCC	Cat#HTB134; RRID:CVCL_0334
Human A13A primary PDAC cells	Elliott et al., 2019.	N/A
Experimental models: Organisms/strains		
Mouse: $NOD\text{-}Prkdc^{em26Cd52}Il2rg^{em26Cd22}/\text{NjuCrl}$ (NCG)	Charles River Laboratories	Cat#572
Oligonucleotides		
human IFNB1 RT-PCR primer-forward (5'-TCACCAGGGGAAAACTCATGAGC-3')	Liang et al., 2021.	N/A
human IFNB1 RT-PCR primer-reverse (5'-GAGATCTTCAGTTTCGGAGGTAACCT-3')	Liang et al., 2021.	N/A
human RRM2 RT-PCR primer-forward (5'-CACAAGGCATCGTTTCAATG-3')	This paper	N/A
human RRM2 RT-PCR primer-reverse (5'-ACAGAAGCCCGCTGTTTCTA-3')	This paper	N/A
human STING-targeting gRNA (5'-AGAGCACACTCTCCGGTACC-3')	This paper	N/A

REAGENT or RESOURCE	SOURCE	IDENTIFIER
Antibodies		
human SAMHD1-targeting gRNA (5-GTCATCGCAACGGGGACGCT-3')	Liang et al., 2021.	N/A
Recombinant DNA		
pMD2G lentiviral packaging plasmid	Addgene	Cat#12259
psPAX2 lentiviral packaging plasmid	Addgene	Cat#12260
LentiCrisprV2 plasmid	Addgene	Cat#52961
pLenti PURO DEST mammalian expression plasmid	Invitrogen	Cat#17452
pENTR-D/TOPO plasmid	ThermoFisher Scientific	Cat#KP240020
pLENTI TetR BLAST mammalian expression plasmid	Addgene	Cat#17492
Software and algorithms		
Flowjo software	Tree Star	https://www.flowjo.com
Graphpad Prism software	Graphpad	https://www.graphpad.com/scientific-software/prism/
Other		
Q-Exactive mass spectrometer	Thermo	N/A
6460 triple quadrupole mass spectrometer	Agilent	N/A
SynergyH1 microplate reader	BioTek	N/A
QuantStudio3 Real-Time PCR system	ThermoFisher Scientific	N/A
IncuCyteZoom live cell imaging system	IncuCyte	N/A